THESIS FOR THE DEGREE OF DOCTOR OF PHILOSOPHY

Phase transitions, scattering and soft dynamics in perovskites

PETTER ROSANDER

Phase transitions, scattering and soft dynamics in perovskites
PETTER ROSANDER

Department of Physics
Chalmers University of Technology
SE-412 96 Gothenburg, Sweden
Telephone +46 (0)31 772 10 00

Cover: Shows an incoming particle and several octahedras.

Figures have been created using Matplotlib [1], OVITO [2], and Inkscape [3]

Phase transitions, scattering and soft dynamics in perovskites

Petter Rosander
Department of Physics
Chalmers University of Technology

Abstract

The study of phase transitions is a critical area of research in condensed matter physics. In the context of this thesis, phase transitions are related to the change of the underlying atomic structure of the material. A phase transition can, e.g., be driven by increasing pressure or temperature and can directly influence the material's properties. Experimentally, the phase transition can be studied via scattering experiments where the phase transition can be detected via, e.g., a new Bragg peak in X-ray diffraction or the appearance of new peaks in Raman scattering. Moreover, the scattering experiments are intimately linked to the vibrational properties of materials. Therefore, it is of high importance to understand the vibrational properties of a material.

In recent years, there has been a surge in efforts to improve the efficiency and accuracy of simulations related to vibrational properties. Consequently, we can now develop interatomic potentials that are both fast to evaluate and highly accurate. These advanced techniques, open up the possibility to study scattering experiments over a wide range of temperatures and pressures and for large systems and long times. In this thesis, density functional theory is employed to generate training data for the construction of such potentials. The potentials are either force constant potentials or neural network potentials. The developed models are subsequently used for lattice dynamics and molecular dynamics simulations. To significantly extend the total simulation time of the molecular dynamics or to reduce the computational time, graphical processing units are utilized.

This thesis then employs such interatomic potentials to, e.g., examine the soft anti-ferrodistortive phonon mode in barium zirconate using self-consistent phonons and molecular dynamics. This soft mode is expected to be the determining factor for which structure $BaZrO_3$ adopts at low temperatures. Moreover, due to the low frequency of this mode, there has been debate about the possibility of emerging local structures associated with the mode. To explore this, we investigated the local dynamics of the octahedral tilt and conducted simulations of the Raman scattering, neutron scattering and electron diffraction. Similar methods were employed to study the phonon dynamics in the highly anharmonic perovskite, $CsPbBr_3$.

Keywords: oxides, perovskites, lattice dynamics, slow dynamics, force constants, density functional theory, anharmonicity, phonons

This thesis is partly based on the author's licentiate thesis (P. Rosander, Lattice dynamics in perovskites for green energy applications A theoretical perspective (2022)). It consists of a background to the field and the following papers:

I   **Anharmonicity of the antiferrodistortive soft mode in barium zirconate BaZrO$_3$**
Petter Rosander, Erik Fransson, Cosme Milesi-Brault, Constance Toulouse, Frédéric Bourdarot, Andrea Piovano, Alexei Bossak, Mael Guennou and Göran Wahnström
Physical Review B **108**, 014309 (2023), Editors' Suggestion
doi: 10.1103/PhysRevB.108.014309

II   **Understanding Correlations in BaZrO$_3$:**
Structure and Dynamics on the Nanoscale
Erik Fransson, Petter Rosander, Paul Erhart, and Göran Wahnström
Chemistry of Materials **36**, 514 (2024)
doi: 10.1021/acs.chemmater.3c02548

III   **Limits of the phonon quasi-particle picture at the cubic-to-tetragonal phase transition in halide perovskites**
Erik Fransson, Petter Rosander, Fredrik Eriksson, Magnus Rahm, Terumasa Tadano and Paul Erhart
Communications Physics **6**, 173 (2023)
doi: 10.1038/s42005-023-01297-8

IV   **Tensorial Properties via the Neuroevolution Potential Framework:**
Fast Simulation of Infrared and Raman Spectra
Nan Xu, Petter Rosander, Christian Schäfer, Eric Lindgren, Nicklas Österbacka, Mandi Fang, Wei Chen, Yi He, Zheyong Fan, and Paul Erhart
Journal of Chemical Theory and Computation **20**, 3273 (2024)
doi: 10.1021/acs.jctc.3c01343

V   **Untangling the Raman spectrum of cubic and tetragonal BaZrO$_3$**
Petter Rosander, Erik Fransson, Nicklas Österbacka Paul Erhart, and Göran Wahnström
Submitted to Chemistry of Materials

The author's contribution to the papers:

I   I performed all DFT calculations. The modelling and analysis were done together with Erik Fransson. The writing of the manuscript was a joint effort.

II I performed all DFT calculations and did the validation of the NEP. The modelling and analysis were done together with Erik Fransson. I wrote parts of the initial draft and proof-read the paper.

III I performed DFT calculations and did the stochastic self-consistent harmonic approximation (SSCHA) and the self-consistent phonon (SCP) with HIPHIVE calculations and I proof-read the paper.

IV I built the training set for the dielectric susceptibility model for $BaZrO_3$, assisted in building of the TNEP model, and did the training of the SA-GPR model. Further, I performed all the Raman spectrum calculation of $BaZrO_3$. Aided in the writing of the Raman and IR spectrum section and I proof-read the paper.

V   I performed all Raman spectrum simulations and the analysis of the decomposed Raman spectrum. Wrote the initial draft of the manuscript and I proof-read the final version.

PUBLICATIONS NOT INCLUDED IN THIS THESIS

The following publications are outside the scope of this thesis:

Elaborating on the vibrational impact of defects on the hydration thermodynamics in $BaZrO_3$
Petter Rosander and Göran Wahnström
In manuscript

Construction and sampling of alloy cluster expansions – A tutorial
Pernilla Ekborg-Tanner, Petter Rosander, Erik Fransson and Paul Erhart
Submitted to *Physical Review X Energy*
doi: 10.48550/arXiv.2405.14787

Beyond the dilute limit: Cluster expansion Y-doped $BaZrO_3$
Petter Rosander, Astrid Marthinsen and Göran Wahnström
In manuscript

List of abbreviations

AFD antiferrodistortive. 7, 8, 32, 33

AIMD ab-initio molecular dynamics. 27, 31, 35

BZO $BaZrO_3$. 2, 3, 7–9, 24–26, 32–34, 40, 44, 45, 53, 60, 61

CPB $CsPbBr_3$. 2, 3, 8

DFT density functional theory. 1, 2, 4, 9, 14, 16, 17, 19, 21, 34, 35

DoS density of states. 23, 28

EHM effective harmonic model. 32, 33, 40

FC force constants. 21, 22, 27, 28, 31, 32, 50, 51

FCP force constant potential. 2, 33, 34, 40

GGA generalized gradient approximation. 15–17

LDA local Density Approximation. 14–17

MD molecular dynamics. 2, 27, 31, 32, 35, 40, 48, 53, 54

RMSE root mean squared error. 49, 50, 54

SCP self consistent phonon. 31–34

TDEP temperature-dependent effective potential. 31–33

XC exchange correlation. 13–16

Contents

1

Introduction

Materials science is a key research area that underpins our modern society. For example, the progress of the modern computer is in part thanks to the improved microscopic understanding of semiconductors. Crucial to material science is the cross-collaboration between theory and experiments. Theoretical computer simulations can guide experiments to materials with enhanced properties but also give deeper insights into experimental observations. Over the past years, the performance of these computer simulations has increased immensely. This is partly thanks to the ability to work collaboratively on software packages, which has improved considerably with the increased connectivity. As a result, research groups now collaborate on a few shared software packages, rather than each group developing its own. This has led to fewer but faster and more advanced computer codes. Alongside the increased connectivity, the computer hardware has become more efficient and significantly faster. Owing to this, the present material science community has been able to run previously prohibitively expensive atomic scale simulations. This opens up the possibility to screen an ever larger pool of materials, or get even deeper insights into experimental observations.

The solution of the Schrödinger equation, which describes the dynamics of systems on the atomic scale, scales extremely poorly with system size. The scaling problem can, e.g., be partly solved with density functional theory (DFT), which have made it possible to use computers to solve the Schrödinger equation for larger systems but the smallest. However, in reformulating the Schrödinger equation we have to pay a price, the electron-electron interaction introduces difficulties that can only be solved approximately. Despite this shortcoming, DFT has proven to be invaluable to materials science and has accelerated the search for optimal materials. For example, DFT allows for calculation of many properties on the atomic scale, such as the total energy and atomic forces. Calculating the forces and energies allows for structure relaxation, i.e., low energy structures can be found, and, e.g., reaction energies can be calculated using

the total energy.

However, despite the increased computational power, and the finesse of DFT, some simulations can still be prohibitively expensive when many degrees of freedom need to be considered. For example, if we were to predict how the properties of a materials changes as we increase the temperature, we would have to solve the Schrödinger equation for all possible arrangements of the atoms, which is not computationally feasible. Fortunately, the recent boom in machine learning has made it possible to develop surrogate models that are not only extremely accurate but also orders of magnitude faster than directly solving the Schrödinger equation. Such models can, e.g., be cluster expansions, neural network potentials or force constant potential (FCP)s. These model are then trained with input from, e.g., DFT. Despite the significantly faster surrogate models, sampling every possible atomic arrangement remains computationally untractable. The solution is then to use methods that sample atomic configurations based on the probability distribution, such as molecular dynamics (MD), path integrals, or Monte Carlo simulations. While its true that DFT can be used directly in these simulations, surrogate models are far more appealing as they enable simulations over much longer time and length scales.

Sustainability is central to this thesis. While we do not directly examine the specific properties related to the materials' usage in the green energy sector, we provide a detailed atomistic description. This detailed atomistic description is essential for a comprehensive understanding of the material and critical for future developments. Then, in the present thesis we study two distinct perovskites $BaZrO_3$ (BZO) and $CsPbBr_3$ (CPB), both of which have potential uses in the green energy sector—BZO in fuel cells and electrolyzers, and CPB in solar cells. We use both DFT and surrogate models to explore the dynamics of these perovskites and draw important conclusion about experimental observations. For instance, we investigate the soft dynamics of the octahedra in both materials, as discussed in Chapter 2.

Fuel cells and electrolyzer is at the core of the hydrogen economy, the purpose of the fuel cell is to convert hydrogen and oxygen gas into electricity and water. This process can also run in reverse, as an electrolyzer, producing hydrogen and oxygen gas by splitting water using electricity. Fig. 1.1 shows the operation of a protonic ceramic fuel cell in fuel cell mode. The anode splits hydrogen gas into protons and electrons, the electron is then carried through an external load while the protons are conducted through the electrolyte. The cathode absorbs the oxygen gas on the surface and the electrons reduces the oxygen, which reacts with the protons to form water. Good performing and durable fuel cells has recently been manufactured [4, 5]. For a more detailed discussion on the protonic ceramic fuel cells, see, e.g., Ref. [6, 7].

When the cell is running in electrolyzer mode, the hydrogen produced can be stored in a multitude of ways, e.g., by liquifying or pressurizing it. The advantage of storing energy in an intermediate form such as hydrogen gas is that the energy can be used much later [8]. Electrolyzers can thus be used in combination with, e.g., solar, wind or
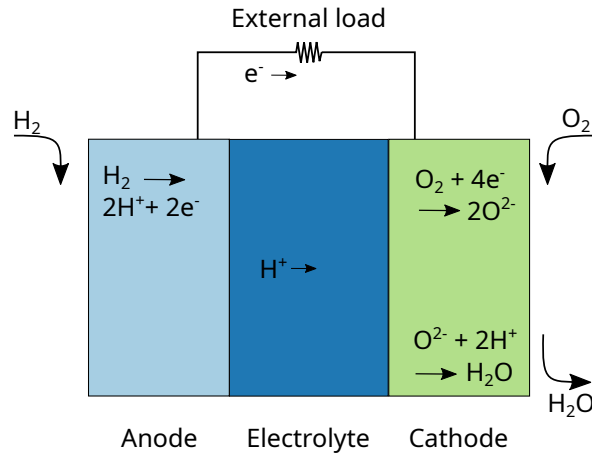
Figure 1.1: Operation of a protonic ceramic fuel cell

hydro energy to store the excess electricity as hydrogen when the demand is low. The hydrogen can then later be used in fuel cells to produce energy when the demand is higher.

As previously mentioned, we studied BZO, which has been shown to be a good candidate material for the electrolyte in fuel cells and electrolyzers. It is an insulator, and it has been shown to be a promising proton conductor when doped with a trivalent anion such as yttrium or scandium [9, 10]. We have explored the dynamics of BZO and focused on the stability of the cubic phase. The stability of the cubic structure is strongly linked to a tilting of the oxygen octahedra. The tilting has also been shown to be related to proton transfer [11, 12].

Solar cells are also important for the green energy transition. The solar cell uses direct sunlight to create a potential across the cell (open circuit voltage), which is typically in the range 1 V.

The working principle of the solar cell is depicted in Fig. 1.2, an electron is excited to the conduction band by photoabsorption, the excited electron is then carried to the electron transport layer and the hole is carried to the hole transport layer, this creates a positive and negative terminal (the open circuit voltage). The positive and negative terminal can then be connected to an external device which allows the electrons and holes to recombine. The power created this way can be directly exported to the electrical grid, or used in symbiosis with the electrolyzer to create hydrogen gas when the demand for power is low. For a more detailed description of solar cells, see, e.g, [13].

As previously mentioned, we also studied the halide perovskite CPB. CPB has been demonstrated to be a candidate material for the photoactive layer in solar cells [14–16]. For the photoactive layer, the critical parameter that we want to tune is the band
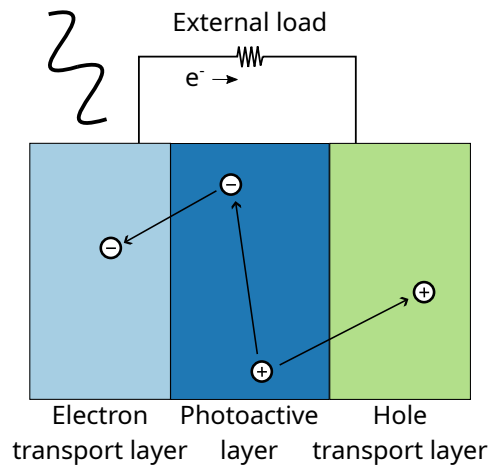
Figure 1.2: Operation of a solar cell

gap. Filip *et al.* [17] found that the band gap of metal-halide perovskites dependence sensitively on the rotation of the halide octahedra. Moreover, they found that this could be controlled by, e g., the size of the cation. Wiktor *et al.* [18] also noticed that the fluctuations' of the octahedra depends sensitively on the temperature, which has a strong impact on the band gap. Therefore, it is of utmost importance to understand the dynamics of these tilt modes in the halide perovskite.

Outline, we will first introduce the perovskite structure, and then, the computational methods used to study these materials. This includes the basics of DFT and a discussion on how the electron-electron interaction is treated on different levels of DFT. Following this will be an introduction to how the nuclei system is treated and how the anharmonicity impacts the system and how it can be dealt with. The next chapter will then describe how we can simulate experimental techniques that probe the nuclei system. I will then introduce different regression and regularization methods, and finally, summarize my work.

2

The perovskite structure

The Prussian mineralogist Gustav Rose discovered a mineral [19] which was given the name Perovskite after the Russian mineralogist Count Lev Perovskiy. The discovery was originally of calcium titanate ($CaTiO_3$), however, many more materials exhibit the same structure, which is now known as the perovskite structure. The chemical formula is ABX_3, where A and B are cations and X an anion. The B cation is 6-fold coordinated with the X anion (octahedron) while the A cation is 12-fold coordinated with the X anion (cuboctahedron). Fig. 2.1 shows the 6-fold coordination of the B cation together with the box of A cations surrounding it. The common representation of the cubic
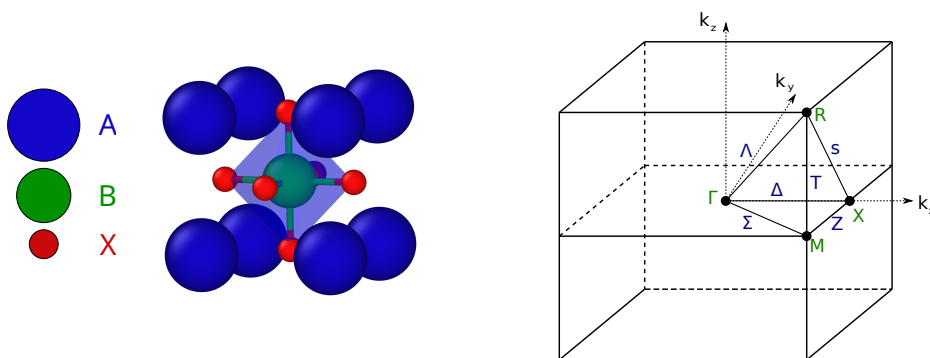

Figure 2.1: The ideal cubic perovskite structure together with the Brillouin zone, which shows the high symmetry points and the paths between them.

perovskite is,

$$\begin{cases} A \sim (0,0,0)a_0 \\ B \sim (0.5, 0.5, 0.5)a_0 \\ X \sim \{(0.5, 0.5, 0)a_0\} \end{cases} \tag{2.1}$$

where a_0 is the lattice constant and { } indicates cyclic permutation. The reciprocal unit cell of the cubic structure including its high symmetry points and the paths connecting these points, is illustrated in Figure 2.1.

There exist a vast number of perovskites owing to the extensive possible paring of the A and B site ions. However, the possible paring of the A and B ions for ionic perovskites is restricted by the charge neutrality condition, the oxidation numbers must sum to zero. For an oxygen perovskite, we have three possible parings of oxidation state for the A and B ions, namely, 1:5, 2:4 and 3:3. Substitutional defects on the A and B sites gives an even larger pool of possible materials, one such class of materials is the high-entropy perovskite oxides [20, 21]. Another class of trending materials is the hybrid perovskites, where the X atom is occupied by a halide anion, e.g., Br. The A site can be occupied by e.g., Cs, but also molecules such as formamidinium. Lastly, the B site is a bivalent metal cation such as Pb. This class of materials are relevant in, e.g., solar cells, photodetectors or nanolasers [22–25].

Thanks to the vast number of materials, the perovskite structure has shown numerous of novel properties, such as, triple conduction of electrons, protons, and oxygens [26], proton conductivity [27], piezoelectricity [28], multiferroicity [29], dielectricity [30] and magnetocalorimetry [31].

2.1 Phases of the perovskite structure

Few perovskites exhibit the ideal cubic structure, most unit cells are instead distorted to, e.g., orthorhombic, tetragonal or trigonal cells. Goldschmidt derived an empirical formula for determining if the perovskite would exhibit the cubic structure or not, the Goldschmidt tolerance factor [32]. Assuming that the perovskite is mostly ionic, we can model the ions as hard spheres. We can then derive the ratio of how well different ionic radii [33] match along different axes of the crystal. Measuring the lattice constant along the B-X axis gives a lattice constant of $a = 2(R_B + R_X)$, whereas measuring along the A-X axis gives $a = \sqrt{2}(R_A + R_X)$. The tolerance factor is then given as the fraction of the lattice constant along different crystal axes,

$$t = \frac{R_A + R_X}{\sqrt{2}(R_B + R_X)}.$$

The closer the tolerance factor is to 1 the more likely it is that the structure will exhibit the ideal cubic structure. However, it is important to remember that the tolerance factor

should serve as a guide and not a rule.

Perovskites with a tolerance factor larger than 1 are usually distorted to a tetragonal or hexagonal lattice, the B ion is too small, and the lattice will develop polar distortions, such as in $BaTiO_3$ [34]. On the other hand, a smaller tolerance factor indicates that the A ion is too small and can't effectively bind with all neighboring oxygen ions. The structure is then commonly distorted to an orthorhombic cell, e.g., $CaTiO_3$, $CdTiO_3$ [35] and $BaCeO_3$ [36].

2.2 Phase transitions in perovskites

Phase transitions can be classified according to the Ginzburg–Landau theory [37]. In essence, the free energy is expanded in terms of an order parameter. The order parameter is a parameter that changes across the phase transition. In the high symmetry phase, the order parameter is, on average, zero, whereas in the low symmetry phase it is non-zero. Thus, if the order parameter were to be tracked as a function of temperature, it would deviate from zero at and below the phase transition.

The order of the phase transition is then classified as either first or continues order. If the change of the order parameter at the phase transition is discontinuous, then it is a first order phase transition, otherwise it is a continues phase transition. The continues phase transitions can also be subclassified as, e.g., second order or tricritical.

$SrTiO_3$ is a perovskite material that has an extensively studied phase transition [38–45]. At ambient pressure, and $\sim 105\,K$ the material undergoes a displacive phase transition. This phase transition has been deemed to be mostly of second order character [44, 45]. However, a more complete analysis reveals that it appears to be somewhere in between a tricritical and second order [39]. The phase transition is driven by the softening of the antiferrodistortive (AFD) mode where successive oxygen octahedra [ZrO_6] are rotated in opposite direction (out of phase), the distortion is depicted in Fig. 2.2. This phase transition has also been shown to be strongly related to the Goldschmidt tolerance factor [46].

The softening results in that thermal diffuse scattering [47] appears at the R-point, slightly above the phase transition temperature. Thermal diffuse scattering is non-Bragg intensities in X-ray and neutron scattering due to large displacements of atoms, usually due to low frequency phonons. However, a sharp, extra peak appear as well, this peak is distinctly different from the thermal diffuse scattering and has been under heavy investigation [38, 40–43]. It is mostly believed that it stems from defects, these defects tend to form regions in the crystal where the material undergoes the phase transition slightly above the phase transition temperature. These regions then contributes a Bragg reflection at the R-point. The idea is not too far from the idea of nanodomains in BZO, that will be discussed in the next section.

It is also worth nothing that $SrTiO_3$ has two unstable phonon modes at $0\,K$, the afore-
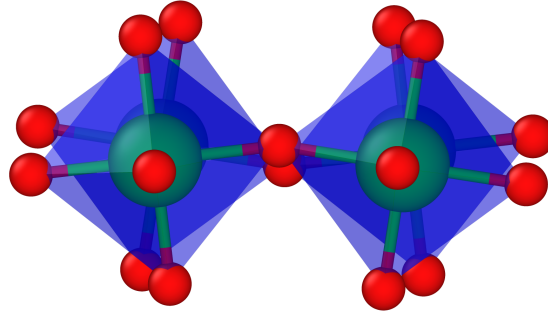
Figure 2.2: A schematic representation of the tilting of the oxygen octahedra. The distortion is exaggerated for visualization purposes.

mentioned AFD mode and a competing soft mode at the zone center. This zone center mode carries a net polarization which corresponds to a ferroelectric phase transition. Zhong and Vanderbilt [46] argues that theses two competing instabilities stabilizes each other. That is, if you could freeze one of the modes, the phase transition temperature of the other would increase. Therefore, they argue that, together with quantum fluctuations, the ferroelectric phase is suppressed by the competition with the ferroelastic phase. Materials that suppress the ferroelectric phase due to quantum fluctuations is sometimes referred to as a quantum paraelectric material. The quantum paraelectricity has also been confirmed experimentally [48]. However, strain engineering can induce the ferroelectric phase transition [49]. Examples of materials that exhibit the ferroelectric phase transition without any strain engineering are, e.g., $BaTiO_3$ [50, 51] and $PbTiO_3$ [52].

Another heavily studied material is CPB [53–56]. CPB is cubic at ~ 400 K and ambient pressures but undergoes two phase transitions as the temperature is lowered [57–60]. It goes from cubic to tetragonal, driven by a similar mode as the one driving the phase transition in $SrTiO_3$. This mode is also a tilt mode, but it is in phase instead of out of phase and is found at the M-point instead of the R-point. It then goes from tetragonal to orthorhombic by a condensation of two AFD modes [61]. The phase transition from cubic to tetragonal is a first order transition, whereas the transition from tetragonal to orthorhombic is a continues transition [57, 61].

2.3   A case study: barium zirconate

A good candidate to preserve the cubic symmetry all the way down to 0 K is BZO, as the tolerance factor is close to 1 (~ 1.01). However, depending on the approximation

used in the DFT calculations, an imaginary frequency at the R-point of the reciprocal lattice appears, this is the same instability as the one found in $SrTiO_3$. It is thus debated whether BZO remains cubic all the way down to 0 K [62–70].

Experimental sintering of BZO is difficult because of its high melting temperature and long soaking times [71]. BZO is therefore commonly studied using powder samples [62, 65, 72]. For example, Akbarzadeh *et al.* [62] studied BZO using x-ray and neutron diffraction on a powder sample together with Monte Carlo simulations using an effective Hamiltonian. They found that the structure remained cubic all the way down to at least 2 K. Perrichon *et al.* [65] found that the cubic phase can be ascribed down to at least 3 K using neutron powder diffraction. They also measured the dynamical structure factor at the R-point at different temperatures and revealed a weak frequency dependence with temperature, which agreed well with the theoretical calculations. The theoretical calculations also revealed that the stability of the cubic structure depended on the approximation used, and that it is very sensitive to the lattice parameter. That is, the stability of the cubic structure correlates strongly with the size of the lattice parameter, a larger cell stabilizes the cubic structure. The dependence of the cubic structure's stability on the approximation used has been observed in other studies as well [66–69] and the correlation with the lattice parameter is corroborated in a study by Yang *et al.* [73]. Yang *et al.* studied BZO at room temperature and high pressures, and found that BZO undergoes a phase transition from cubic to tetragonal when the pressure is increased.

Furthermore, Toulouse *et al.* [70] and Chemarin *et al.* [74] investigated the Raman spectrum of BZO. The Raman spectrum should be completely absent for a cubic structure due to the selection rules of first order scattering. However, both studies found that the Raman spectrum exhibited peaks, contrary to the selection rules. Therefore, Chemarin *et al.* attributed these peaks to locally tilted nanodomains. Whereas, Toulouse *et al.* attributed a majority of the peaks to unusually sharp overtones, which is a higher order process. Giannici *et al.* [63] also performed Raman spectroscopy as well as x-ray diffraction experiments on BZO and Y doped BZO. They also noticed the peaks in the Raman spectrum for undoped BZO. However, as the x-ray diffraction was consistent with the cubic structure, they attributed the peaks to locally distorted domains due to the tiling of the oxygen octahedra, i.e., they came to the same conclusion as Chemarin and others. Similarly, Levin *et al.* [64] observed evidence for a local symmetry reduction. They studied BZO using a transmission electron microscope and observed a weak but yet discrete spot at the R-point. The spot appeared below 80 K and they suggested that this may be evidence of the existence of nanodomains below this temperature.

Electronic structure theory

The Schrödinger equation describes the dynamics of systems on the atomic scale. It gives physical insight into both the structural and chemical properties of materials. However, solving it for even the smallest system is a formidable task. The time-independent Schrödinger equation is usually written in a deceptively simple form,

$$\mathscr{H}\Psi_n(\mathbf{R}, \mathbf{x}) = \mathscr{E}_n\Psi_n(\mathbf{R}, \mathbf{x}).$$

where $\Psi_n(\mathbf{R}, \mathbf{x})$ is the wave function, $\mathbf{R}$ encodes the nuclear positions and $\mathbf{x}$ describes the spin, σ, and position, $\mathbf{r}$, of the electrons, $\mathscr{E}_n$ is the energy of the system. The Hamiltonian $\mathscr{H}$ includes a description of all interactions that are taken into account. It is conveniently written in atomic units, where the mass and charge of the electron together with $\hbar$ and $4\pi\epsilon_0$ is set to 1. In the absence of any external fields it reads,

$$\mathscr{H} = -\sum_i \frac{\nabla_i^2}{2} + \frac{1}{2}\sum_{i \neq j} \frac{1}{|\mathbf{r}_i - \mathbf{r}_j|} - \sum_k \sum_i \frac{Z_k}{|\mathbf{R}_k - \mathbf{r}_i|}$$
$$- \sum_k \frac{\nabla_k^2}{2m_k} + \frac{1}{2}\sum_{k \neq n} \frac{Z_k Z_n}{|\mathbf{R}_k - \mathbf{R}_n|},$$

where m_k and Z_k is the mass and charge of the kth nucleus. The first and fourth term is the kinetic energy of the electronic and nuclear system, the other terms are the Coulomb interactions. For example, the second term is the repulsion between the electrons, which presents most of the difficulty. This equation is separated into two decoupled equations by assuming that the electronic system reacts instantaneously to any change in the ionic system due to the much smaller mass of the electrons. This is what is known as the Born-Oppenheimer (or adiabatic) approximation [75] and leads

to the following Hamiltonian for the electronic system,

$$\mathcal{H}_{\text{el}} = -\sum_i \frac{\nabla_i^2}{2} + \frac{1}{2} \sum_{i \neq j} \frac{1}{|\mathbf{r}_i - \mathbf{r}_j|} - \sum_k \sum_i \frac{Z_k}{|\mathbf{R}_k - \mathbf{r}_i|}, \tag{3.1}$$

where the ionic position is fixed and represents an external potential. The ionic system is treated in Chapter 4. This equation is still only possible to solve for the smallest systems, as the size of the Hamiltonian grows factorially with the number of electrons [76]. Thus, further simplifications are needed.

3.1 The Hohenberg-Kohn theorem

Hohenberg and Kohn [77] recognized that the ground state density of the Hamiltonian in Eq. (3.1) is uniquely defined by the external potential. Therefore, they concluded that we may work with the electron density instead of the wave function, which means that the problem has been reduced to a problem of three dimensions. The corresponding energy functional is then given by,

$$\begin{aligned} \mathcal{E}_{HK} &= \langle \Psi[n(\mathbf{r})]|\mathcal{H}_{\text{el}}|\Psi[n(\mathbf{r})]\rangle \\ &= T[n(\mathbf{r})] + V[n(\mathbf{r})] + \int d\mathbf{r}\, n(\mathbf{r})V_{\text{ext}}(\mathbf{r}). \end{aligned} \tag{3.2}$$

The kinetic energy functional, $T[n(\mathbf{r})]$, and electron Coulomb interaction, $V[n(\mathbf{r})]$, are system independent. Therefore, in principle, they could be determined once and then be applied to all systems. However, the exact functional form is still unknown.

The variational principle tells us that the density that minimizes the energy functional in Eq. (3.2) is the true ground state density. This minimization is constrained by the normalization of the electron density,

$$\int d\mathbf{r}\, n(\mathbf{r}) = N,$$

where N is the total number of electrons. Hohnberg and Kohn only proved that we may work with the density to find the ground state energy. However, they provided no computational strategy on how to solve the minimization problem.

Hohnberg and Kohn were not the only ones who proposed that one could work with a density functional. Previous work by, e.g., Thomas [78], Fermi [79] and Dirac [80] also explored this possibility.

3.2 The Kohn-Sham formulation

Fortunately, Kohn and Sham provided an algorithmic scheme on how to solve the minimization problem. The idea behind the Kohn-Sham computational scheme [81] is that

an effective potential in a non-interacting auxiliary system can be used to mimicking the interacting system. That is, they sought an effective potential, $V_{\text{eff}}(r)$, that represents the interactive system such that a single particle equation,

$$\left[-\frac{1}{2}\nabla^2 + V_{\text{eff}}(r) \right] \psi_n(r) = \varepsilon_n \psi_n(r), \tag{3.3}$$

can be solved instead. The corresponding energy functional for this non-interacting auxiliary system is then,

$$\mathscr{E}_s[n(\mathbf{r})] = T_s[n(\mathbf{r})] + \int d\mathbf{r} \; V_{\text{eff}}(\mathbf{r})n(\mathbf{r}), \tag{3.4}$$

where $T_s[n(\mathbf{r})]$ is the kinetic energy of the non-interacting system. Another key insight that Kohn and Sham had was to rewrite the energy functional in Eq. (3.2) as,

$$\mathscr{E}[n(\mathbf{r})] = T_s[n(\mathbf{r})] + \frac{1}{2}\int d\mathbf{r}' \; \frac{n(\mathbf{r})n(\mathbf{r}')}{|\mathbf{r}-\mathbf{r}'|} + \mathscr{E}_{xc}[n(\mathbf{r})] + \int d\mathbf{r} \; V_{\text{ext}}(\mathbf{r})n(\mathbf{r}), \tag{3.5}$$

where the kinetic energy of the non-interacting system, $T_s[n(\mathbf{r})]$, and the Hartree term, the second term, have been added and subtracted. The exchange correlation (XC) energy functional, $\mathscr{E}_{xc}[n(\mathbf{r})]$, has also been introduced which is defined as,

$$\mathscr{E}_{xc}[n(\mathbf{r})] = T[n(\mathbf{r})] - T_s[n(\mathbf{r})] + V[n(\mathbf{r})] - \frac{1}{2}\int \frac{n(\mathbf{r})n(\mathbf{r}')}{|\mathbf{r}-\mathbf{r}'|}d\mathbf{r}d\mathbf{r}'. \tag{3.6}$$

The functional derivative of this energy is denoted, $V_{xc}[n(\mathbf{r})]$, and referred to as the XC potential. The effective potential is now found by calculating the functional derivative of the energy functionals and comparing the results, the derivatives are given by

$$\frac{\delta \mathscr{E}_s[n(\mathbf{r})]}{\delta n(\mathbf{r})} = \frac{\delta T_s[n(\mathbf{r})]}{\delta n(\mathbf{r})} + V_{\text{eff}}(\mathbf{r})$$

$$\frac{\delta \mathscr{E}[n(\mathbf{r})]}{\delta n(\mathbf{r})} = \frac{\delta T_s[n(\mathbf{r})]}{\delta n(\mathbf{r})} + V_{\text{ext}}(\mathbf{r}) + V_{xc}[n(\mathbf{r})] + \int \frac{n(\mathbf{r}')}{|\mathbf{r}-\mathbf{r}'|}d\mathbf{r}'.$$

From these two equations it is easily seen that it is possible to map the auxiliary non-interacting system to the interacting system by setting

$$V_{\text{eff}}(\mathbf{r}) = V_{\text{ext}}(\mathbf{r}) + V_{xc}[n(\mathbf{r})] + \int \frac{n(\mathbf{r}')}{|\mathbf{r}-\mathbf{r}'|}d\mathbf{r}'. \tag{3.7}$$

The last thing to note is that the energy functional of the auxiliary non-interacting system is not the same as the interacting system. Inserting Eq. (3.7) into Eq. (3.4) and matching with Eq. (3.5) we can see that we need to subtract half of the Hartree energy,

add the XC energy and subtract the integral involving the XC potential which yields
the total energy as,

$$E = \sum_{k=1}^{N} \varepsilon_n - \frac{1}{2} \int \frac{n(\mathbf{r})n(\mathbf{r}')}{|\mathbf{r} - \mathbf{r}'|} d\mathbf{r} d\mathbf{r}' + \mathscr{E}_{xc}[n(\mathbf{r})] - \int d\mathbf{r}\, V_{xc}[n(\mathbf{r})]n(\mathbf{r}), \qquad (3.8)$$

where the sum is over occupied Kohn-Sham orbitals. Hence, the many body Schrödinger
equation has been transformed into a non-interacting single particle equation with an
effective potential. However, we have paid a price in doing so, the effective potential
depends on the density, which in turn depends on the single particle states. Therefore,
we have to solve the equations self-consistently. The solution is as follows, make an
initial guess of the density, calculate the effective potential Eq. (3.7) and then solve
the non-interacting equation Eq. (3.3). The non-interacting equation provides us with
a new set of wave functions, and from these wave functions we can calculate a new
density,

$$n(\mathbf{r}) = \sum_{n=1}^{N} |\psi_n(\mathbf{r})|^2. \qquad (3.9)$$

Now that we have a new density, we can repeat the process until the difference in en-
ergy, Eq. (3.8), between two successive iteration is sufficiently small. For the interested
reader, excellent reviews of the DFT framework are outlined in [82–84].

Lastly, it is important to note that we moved all of our ignorance about the electron-
electron interaction and the kinetic energy into one term, the XC functional, which we
need an approximation for.

3.3 Local density approximation

In the previous section, we outlined how Kohn and Sham wrote down the fundamen-
tals of solving the Schrödinger equation in the Born-Oppenheimer approximation. We
wrote down the equations that can be used to find the ground state energy and density.
However, we still have to find an approximation of the XC energy. The first devised XC
energy functional, given in Eq. (3.6), is the local Density Approximation (LDA) which
assumes that the density varies slowly such that we may approximate the potential as
local, i.e., it depends only on the density at $\mathbf{r}$. However, note that the true potential
will be non-local and not only depend on the density at $\mathbf{r}$ but also on all other points $\mathbf{r}'$.
This approximation leads to the XC energy as

$$\mathscr{E}_{xc}[n] = \int \epsilon_{xc}[n(\mathbf{r})]n(\mathbf{r})d\mathbf{r}.$$

where ϵ_{xc} is the XC energy per particle of the homogeneous system with density $n(\mathbf{r})$.
Even with this approximation, no analytical form of ϵ_{xc} is known. However, ϵ_{xc} can be

separated into an exchange and correlation term. The exchange term is straight forward to derive, see, e.g., [76]. As the name suggests, the interaction involves the exchange of two electrons, which leads to a lowering of the energy. The reduction in energy is rooted in the antisymmetrization of the wave function, which is a materialization of the Pauli exclusion principle. The antisymmetrization keeps electrons with parallel spin apart. Therefore, the effect of the exchange term can be though of as every spin up (spin down) electron having a small bubble of deficient spin up (spin down) that follows the electron around, this effect is called the *exchange hole*. The lowering of the energy can thus be interpreted as the interaction of the electron with the positive *exchange hole* surrounding it [85].

However, in the exchange energy, all other interactions have been ignored. These interactions are collectively called correlation. The correlation energy also lowers the energy, and one can think of a *correlation hole* similarly to the *exchange hole*. In addition to keeping electrons of the same spin apart, the *correlation hole* keeps electrons of antiparallel spins apart as well. It is evident that the correlation is much more important for antiparallel spins than for parallel spins, which are mostly covered by the exchange energy. Analytic expression for the correlation energy can be calculated at low and high density limits [86–88], but there exist no analytical form in between the two limits. For typical solids, the correlation energy is much smaller than the exchange energy, however, as the density decreases the correlation energy becomes more important and even dominates for very low densities.

Different parametrizations of the XC energy have been suggested based on the derived exchange and correlation energy. However, most of them are founded on the diffusion Monte Carlo calculations by Ceperley and Alder [89], which are numerically exact. Moreover, a neat detail of the diffusion Monte Carlo simulations is that they include the kinetic energy, which there exist no analytic expression for, except for a few limited cases, such as the free electron gas. Finally, despite the simplicity of LDA very accurate results have been obtained in, e.g., metallic systems where the density does not vary rapidly. The expressions for the XC energy is readily available in, e.g., Ref. [76].

3.4 Generalized gradient approximation

A natural extension to the LDA is to include derivatives of the density, which should better account for the density variations found in real materials. This family of functionals is termed, generalized gradient approximation (GGA). The exchange correlation energy is then written as,

$$\mathscr{E}_{xc}[n] = \int f[n(\mathbf{r}), \nabla n(\mathbf{r})]d\mathbf{r}.$$

15

Unintuativley, inclusion of the gradient initially made the results worse. However, inclusions of constraints such as, e.g., sum rules and known features about the *exchange* and *correlation hole* resulted in satisfactory functionals. One such functional and probably the most widely used in materials science is the PBE functional parametrized by Perdew, Burke and Ernzerhof [90].

The GGAs can also be parametrized by empirical fitting to known experimental results. However, this leads to poor transferability, and it is not obvious that the experimental results are reproduced due to the correct physics. An excellent discussion on the empirical versus constrained parametrization can be found in Ref. [91].

3.5   Overdelocalization and band gap problem

The Hartree term introduced in the exchange correlation functional, Eq. (3.6), is unphysical in a sense, the electron interacts with a density which itself is a part of. In theory, this interaction should be completely corrected for if we had a complete description of the XC functional. However, since we only have approximations of it, we are left with an issue, the electron interacts with itself. The self interaction, leads to an over-delocalization of the electrons. Corrections to the self interaction can, e.g., improve the predicted band gaps [92]. But, despite the improved band gap with self interaction corrections, it has been argued that the band gap problem would not be solved even with an exact XC description. Rather, one would have to go beyond DFT to solve the problem [93]. The band gap problem is thoroughly discussed in, e.g., Ref. [94].

3.6   DFT + U

One way of treating the over-delocalization issue known to LDA and the GGAs is DFT + U. The method stems from the Hubbard model, which is an approximate model that is used to describe the phase transition from metal to insulator of a solid-state system. The model Hamiltonian is written as,

$$\mathcal{H} = -t \sum_{\langle AB \rangle, \sigma} (c_{A\sigma}^{\dagger} c_{B\sigma} + c_{B\sigma}^{\dagger} c_{A\sigma}) + U \sum_{i} c_{i\uparrow}^{\dagger} c_{i\uparrow} c_{i\downarrow}^{\dagger} c_{i\downarrow}$$

where the first term is the hopping of the electrons between sites, $\langle AB \rangle$ indicates that it is a sum over nearest neighbor pairs A and B. The second part represent the electron-electron repulsion and is important for strongly correlated materials, i.e., there is an associated cost of placing electrons on the same site. The transfer, or hopping integral, t, is related to the crystal potential and kinetic energy as,

$$t = \int d\mathbf{r} \, \psi_A^*(\mathbf{r}) \left[-\frac{1}{2m} \nabla^2 + V(\mathbf{r}) \right] \psi_B(\mathbf{r}).$$

Incorporating this formalism in DFT then gives the energy functional as [95],

$$\mathscr{E} = \mathscr{E}_{\text{DFT}} + \frac{U_{\text{eff}}}{2} \sum_\sigma Tr(\rho_\sigma) - Tr(\rho_\sigma \rho_\sigma),$$

where ρ_σ is the atomic orbital occupation matrix. In the solid-state community the occupation matrix is commonly calculated by projecting the plane waves onto a localized basis set [96]. The interaction will force the orbital to either be fully occupied or fully unoccupied.

A significant benefit of the DFT + U formalism is that it does not significantly increase the computational cost. However, the model is not transferable between systems as the U parameter is system dependent. That is, there is no "universal" way of determining a U parameter that should be suitable for all materials. However, there are ways of determining it theoretically for a specific system, see, e.g., Ref. [96, 97]. For an excellent in depth review of the DFT + U approach, see, e.g., Ref. [96].

3.7 Hybrid functionals

A more system independent way of treating the known over-delocalization of the electrons in DFT is to incorporate exact exchange [98]. The idea is that, if we incorporate some exact exchange energy from the Hartree-Fock theory, we can correct for the over-delocalization of, e.g., LDA or the GGAs. The exact exchange energy is given by [99],

$$\mathscr{E}_x^{\text{HF}} = \sum_{ab} f_a f_b \int \mathrm{d}^3 \mathbf{r}' \, \mathrm{d}^3 \mathbf{r} \, \frac{\psi_a^*(\mathbf{r}) \psi_b^*(\mathbf{r}) \psi_b(\mathbf{r}') \psi_a(\mathbf{r}')}{|\mathbf{r} - \mathbf{r}'|} \tag{3.10}$$

where f_a and f_b is the occupation of orbital a and b. The energy functional that is used in, e.g., PBE0 [98], which is a hybrid functional is then defined as,

$$\mathscr{E} = \frac{1}{4} \mathscr{E}_x^{\text{HF}} + \frac{3}{4} \mathscr{E}_x^{\text{PBE}} + \mathscr{E}_c^{\text{PBE}}.$$

The fraction of mixing, ¼, of the exact exchange has been determined theoretically. The orbital dependence in Eq. (3.10) leads to a significant increase in computational cost. To reduce the computational cost for extended systems but still maintain good accuracy, it has been suggested that the Coulomb kernel can be separated into a long range and short range part. One such functional is HSE06 [100] where the Coulomb kernel is separated in the following way,

$$\frac{1}{|\mathbf{r} - \mathbf{r}'|} = \frac{\text{erf}(\mu|\mathbf{r} - \mathbf{r}'|)}{|\mathbf{r} - \mathbf{r}'|} + \frac{\text{erfc}(\mu|\mathbf{r} - \mathbf{r}'|)}{|\mathbf{r} - \mathbf{r}'|},$$

μ controls the screening, and is given by 0.2 for HSE06. The first term is then the short range part, and the second term is the long range part. The energy functional is then given as,

$$\mathscr{E} = \frac{1}{4}\mathscr{E}_x^{\text{HF,SR}} + \frac{3}{4}\mathscr{E}_x^{\text{PBE,SR}} + \mathscr{E}_x^{\text{PBE,LR}} + \mathscr{E}_c^{\text{PBE}}.$$

3.8   Basis functions and pseudopotentials

In practice, the wave functions in the Kohn-Sham equation Eq. (3.3) can be found by solving the equation on a grid. However, for extended systems such as the systems in this thesis, this method would be computational impractical. Instead, a basis set is introduced such that the wave functions can be represented as,

$$\Psi_i(r) = \sum_j c_{ij}\phi_j,$$

where ϕ_j can be chosen in a few different ways. The introduction of the basis functions maps a continuous problem into a problem of linear algebra. Therefore, the problem reduces to finding the expansion coefficients c_{ij}. The choice of basis function depends on the problem, a natural choice for extended periodic systems is, e.g., plane waves,

$$\Psi_{i,\mathbf{k}}(r) = \sum_{\mathbf{G}} c_{i,\mathbf{k}}(\mathbf{G})\exp\left(i\mathbf{r}\cdot(\mathbf{k}+\mathbf{G})\right),$$

where the periodicity is implicitly implied. Plane waves form a complete basis, however, for practical calculation we have to truncate the expansion at some point. This is done via the kinetic energy, $\frac{1}{2}|\mathbf{k}+\mathbf{G}|^2 < E_{\text{cut}}$, such that all plane waves fulfilling the criteria are included. It is thus straight forward to increase the size of the basis set and thus increase the accuracy of the calculation.

Unfortunately, the orthogonality requirement of the wave functions leads to rapid oscillations in the core region of the valance electrons. Consequentially, the kinetic energy of the valance electrons will be large, and by necessity a sizable E_{cut} has to be chosen. A computational tractable way to handle the rapid oscillations is to introduce a pseudopotential [101]. The idea is to construct a pseudowave function where the rapid oscillations of the valance states in the core region has been removed. Moreover, by construction, these pseudowave functions ensures that the valance states remain orthogonal to the core states. Furthermore, given that the pseudopotential is carefully constructed, the correct energy eigenvalues should be obtained.

Exactly how the pseudopotential is constructed varies. For example, how many states that are treated as core states and how large the core radius is can vary depending on the application. Usually, a few different potentials are constructed, and the user decided which potential to use based on the accuracy required. The only necessity is

that the pseudopotential should be constructed such that the pseudowave function coincides with the true wave functions outside the core region. Therefore, a few different implementations of pseudopotentials have been proposed such as norm-conserving, ultrasoft and projector augmented wave (PAW) potentials [102–104]. The PAW method allows us to reconstruct the true wave function in the core region, and this is also the formalism together with plane waves that has been employed in all the DFT calculations in this thesis.

4

Vibrational motion

In this chapter, we will discuss the motion of the nuclei. The Hamiltonian is given by,

$$\mathcal{H} = \sum_i \frac{\mathbf{P}_i^2}{2m_i} + V(\dots, \mathbf{R}_i, \dots) \tag{4.1}$$

where $\mathbf{P}_i$ is the momentum, m_i the mass, and $\mathbf{R}_i$ the position coordinate of atom i. When the system is a crystal, it is convenient to write the atomic positions as,

$$\mathbf{R}_i = \mathbf{R}_i^0 + \mathbf{u}_i, \tag{4.2}$$

where $\mathbf{R}_i^0$ is the equilibrium position and $\mathbf{u}_i$ the displacement from the equilibrium position.

4.1 Force constants

The potential energy $V(\dots, \mathbf{R}_i, \dots)$ in Eq. (4.1) can be expanded as a Taylor series,

$$V = V_0 + \Phi_i^\alpha u_i^\alpha + \frac{1}{2!}\Phi_{ij}^{\alpha\beta} u_i^\alpha u_j^\beta + \frac{1}{3!}\Phi_{ijk}^{\alpha\beta\gamma} u_i^\alpha u_j^\beta u_k^\gamma + \dots, \tag{4.3}$$

where Einstein summation is implied and the Φs are referred to as force constants (FC). Latin indices run over atomic labels and Greek letters run over Cartesian coordinates. The first term, $V_0 = V_0(\dots, \mathbf{R}_i^0, \dots)$, is the energy at the equilibrium positions and can be obtained from, e.g., a DFT calculation. Here, we will set this reference energy equal to zero. Moreover, as we are expanding around the equilibrium positions, the second term is zero by construction. The equilibrium positions may, however, correspond to a saddle point configuration, not necessarily a minimum, but also in that case, the second

term is zero. Construction of models can then be done based on the third and higher terms. Finally, the FCs are defined as derivatives of the potential with respect to the displacements,

$$\Phi_i^\alpha = \frac{\partial V}{\partial u_i^\alpha}, \quad \Phi_{ij}^{\alpha\beta} = \frac{\partial^2 V}{\partial u_i^\alpha \partial u_j^\beta}, \quad \ldots,$$

and the atomic forces F_i^α can be written in terms of the FCs as,

$$F_i^\alpha = -\frac{\partial V}{\partial u_i^\alpha} = -\Phi_{ij}^{\alpha\beta} u_j^\beta - \frac{1}{2}\Phi_{ijk}^{\alpha\beta\gamma} u_j^\beta u_k^\gamma - \ldots. \tag{4.4}$$

4.1.1   Extracting force constants

A common approach to extract the harmonic FC is to use finite displacements, the frozen phonon method. That is, you displace one atom at the time and calculate the FC as [105],

$$\Phi_{ij}^{\alpha\beta} = -\frac{F_i^\alpha}{\Delta u_j^\beta}, \tag{4.5}$$

where Δu_j^β is the finite displacement of atom j in direction β. The extension to higher orders is straightforward, but the number of calculations needed grows quickly. This method also becomes increasingly inefficient as the symmetry decreases.

A more computationally tractable method is to displace all atoms in the cell and recast equation (4.4) into a regression problem,

$$\mathbf{A\Phi} = \mathbf{F}, \tag{4.6}$$

where $\mathbf{A}$ is the design matrix that encodes all displacements, $\mathbf{F}$ are the corresponding forces and $\mathbf{\Phi}$ is a vector of the FCs. HIPHIVE[106] can be used to construct the regression problem, where the underlying symmetry of the system is utilized to reduce the number of independent FCs. To minimize the number of reference calculations and getting physical FCs, we want the regression problem (4.6) to be as well posed as possible. That is, we want the structures to be as uncorrelated as possible, and hopefully have displacement patterns that are highly probable. In theory, the sum in Eq. (4.4) is infinite. Fortunately, the Taylor expansion can commonly be truncated at relatively low expansion order. Moreover, the interactions usually decay rapidly with increasing distance and number of bodies involved. Therefore, only a limited number of FCs needs to be considered in the regression problem.

4.2 Harmonic approximation

The *harmonic approximation* is obtained by truncating the expansion in Eq. (4.3) at the second order term,

$$V = \frac{1}{2}\Phi_{ij}^{\alpha\beta}u_i^\alpha u_j^\beta.$$

The coupled dynamics of the displacements u_i^α can then be transformed into a set of *independent* collective harmonic oscillators, often denoted *normal modes*, by diagonalising the force constant matrix $\Phi_{ij}^{\alpha\beta}$.

4.2.1 Normal modes

We are considering crystalline solids, where the atoms are arranged in an ordered microscopic structure, forming a crystal lattice that extends in all directions. A *unit cell* is introduced, containing n_a atoms, which is repeated periodically in all three directions. The dynamics of the system can then be solved in reciprocal space, $\mathbf{q}$-space, by solving the eigenvalue equation [76],

$$D(\mathbf{q})\,\mathbf{e}_{\mathbf{q}\nu} = \omega_{\mathbf{q}\nu}^2\,\mathbf{e}_{\mathbf{q}\nu}, \tag{4.7}$$

where $D(\mathbf{q})$ is the dynamical matrix, $\omega_{\mathbf{q}\nu}$ the frequency, and $\mathbf{e}_{\mathbf{q}\nu}$ the corresponding eigenvector, or normal mode coordinate. The size of the dynamical matrix is $3n_a \times 3n_a$ and the eigenvalue equation has to be solved for each $\mathbf{q}$ vector in the Brillouin zone, the unit cell in reciprocal space. The index $\nu = 1, \dots, 3n_a$ is called the branch index. More explicitly, the dynamical matrix can be written as

$$D_{\kappa\kappa'}^{\alpha\beta}(\mathbf{q}) = \sum_{l'} \frac{\Phi_{0\kappa;l'\kappa'}^{\alpha\beta}}{\sqrt{m_\kappa m_{\kappa'}}} \exp\left[-i\mathbf{q}\cdot\left(\mathbf{R}_{0\kappa}^0 - \mathbf{R}_{l'\kappa'}^0\right)\right]. \tag{4.8}$$

The atomic index i has here been decomposed as $i = (l\kappa)$, where l and κ are labels of unit cells and atoms in each unit cell, respectively.

The frequencies obtained in the diagonalization of the dynamical matrix are commonly presented in a density of states (DoS) figure. The DoS,

$$g(\omega) = \frac{1}{N_q}\sum_{\mathbf{q}\nu}\delta(\omega - \omega_{\mathbf{q}\nu}), \tag{4.9}$$

counts the number of states available at a given frequency. We have, here, divided with N_q, the number of $\mathbf{q}$-points in the summation. This implies that $g(\omega)$ is normalized such that the integration over frequency becomes $3n_a$. We can also determine the density of states of a single atomic type,

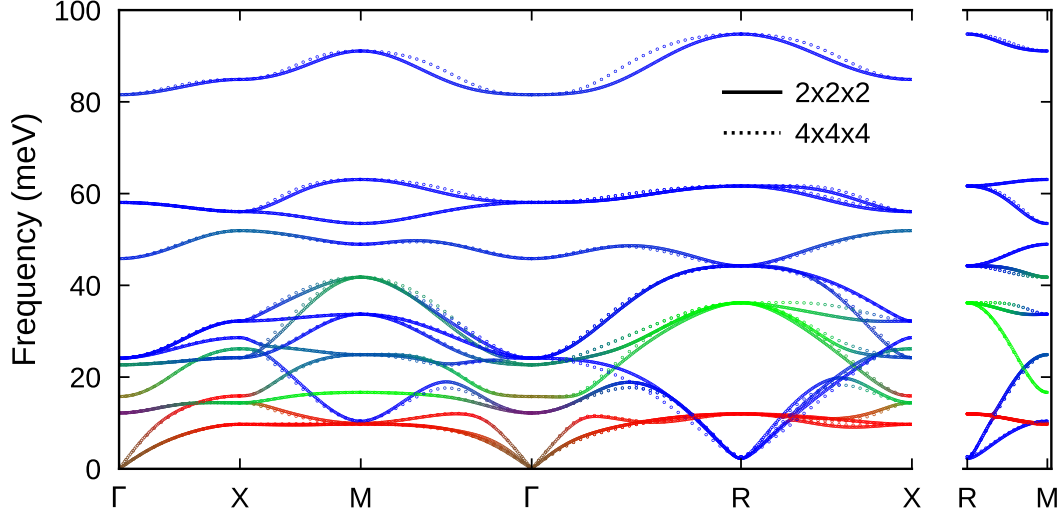$$g_A(\omega) = \frac{1}{N_q}\sum_{\mathbf{q}\nu} c_A(\mathbf{q},\nu)\delta(\omega - \omega_{\mathbf{q}\nu})$$

Figure 4.1: Phonon dispersion for BZO using PBE. Data are shown between high symmetry points and are derived using PHONOPY for a $2 \times 2 \times 2$ and a $4 \times 4 \times 4$ supercell, respectively. Color assigned as (Ba, Zr, O) = (R, G, B).

where

$$c_A(\mathbf{q}, \nu) = \sum_{i \in A} \sum_{\alpha} |\hat{\mathbf{n}}_{i\alpha} \cdot \mathbf{e}_{\mathbf{q}\nu}|^2$$

is how much atomic type A contributes to the normal mode. Here $\hat{\mathbf{n}}_{i\alpha}$ is a unit projection vector of atom i in direction α, and the sum over i is taken over all atoms of type A.

The frequency along the paths between the high symmetry points in the Brillouin zone can be plotted in what is referred to as a dispersion plot. This is shown in Fig. 4.1 for BZO using the PBE functional. The unit cell (5 atoms) is cubic with size a_0=4.24 Å and the calculations are done using PHONOPY. For the definition of the high symmetry points, see Fig. 2.1. The color coding is (Ba, Zr, O) = (R, G, B), which implies that, e.g., a pure oxygen mode will be colored blue and mixed modes will have a mixed color. The direct method introduced by Parlinski *et al.* [107] is used with individual atomic displacements with size 0.01 Å. The size of the computational cell, the supercell, is $2 \times 2 \times 2$ of the unit cell and the LO-TO splitting is included following Ref. [108]. The direct method in Ref. [107] will give the exact frequencies at high symmetry points, due to the use of the $2 \times 2 \times 2$ supercell. Interpolation between these high symmetry points is carried out and if the range of the physical interaction is within half of the supercell size, then the interpolation scheme gives the correct frequencies also in between the high symmetry points.

To test the accuracy with respect to the range of the physical interaction between the atoms, we have also done the calculations for a $4 \times 4 \times 4$ supercell. The result is shown as dotted lines in Fig. 4.1. The two calculations agree at the high symmetry points, and in between the differences are only a few meV. We conclude that a supercell with size $4 \times 4 \times 4$ should be sufficient with respect to range of the physical interaction.

4.2.2 Thermodynamics and phonons

The thermal properties of the vibrational motion can be obtained from statistical mechanics. The motion is quantized, and the normal mode becomes a quasiparticle, a *phonon*. The canonical partition function for the phonon system is given by [109]

$$Z = \prod_{\mathbf{q}\nu} \frac{\exp\left(-\beta\hbar\omega_{\mathbf{q}\nu}/2\right)}{1 - \exp\left(-\beta\hbar\omega_{\mathbf{q}\nu}\right)}. \tag{4.10}$$

where $\beta = 1/k_B T$. The energy is then given by

$$U(T) = -\frac{\partial}{\partial\beta}\ln Z$$

$$= \sum_{\mathbf{q}\nu}\left(\frac{1}{2} + \frac{1}{\exp\left(\beta\hbar\omega_{\mathbf{q}\nu}\right) - 1}\right)\hbar\omega_{\mathbf{q}\nu} \tag{4.11}$$

and by using the expression for the density of states in Eq. (4.9) the sum can be replaced by an integral

$$U(T) = \int_0^\infty g(\omega)\,d\omega\left(\frac{1}{2} + \frac{1}{\exp\left(\beta\hbar\omega\right) - 1}\right)\hbar\omega$$

$$= \int_0^\infty g(\omega)\,d\omega\left(\frac{1}{2} + \langle n(\omega, T)\rangle\right)\hbar\omega\,. \tag{4.12}$$

In the last line the Bose-Einstein distribution $\langle n(\omega, T)\rangle$ is introduced, the mean occupancy of the state with frequency ω at temperature T. In the same way, the entropy is given by

$$S(T) = -k_B\,\beta^2\frac{\partial}{\partial\beta}\left(\frac{1}{\beta}\ln Z\right)$$

$$= k_B\int_0^\infty g(\omega)\,d\omega\left(\frac{\beta\hbar\omega}{\exp\left(\beta\hbar\omega\right) - 1} - \ln\left(1 - \exp\left(-\beta\hbar\omega\right)\right)\right)\,. \tag{4.13}$$

and the Helmholtz free energy F is then obtained from the relation

$$F(T) = U(T) - T S(T)\,. \tag{4.14}$$

In Fig. 4.2 the computed temperature dependence for the energy, entropy and free energy for BZO using PBE is depicted. The energy and entropy increases as function of temperature, while the free energy decreases.
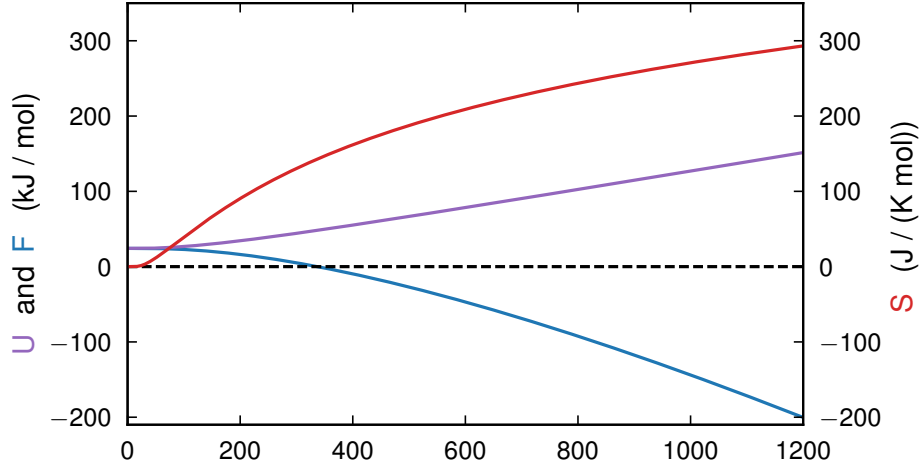
Figure 4.2: The thermal energy U, entropy S and free energy F as function of temperature for BZO.

4.2.2.1 Dynamics of the harmonic system

The atomic displacement operator can be expressed as [105], where the time-dependence can be derived from Heisenberg's equation of motion [110],

$$\hat{u}_{l\kappa}^{\alpha}(t) = \frac{1}{\sqrt{N_q}} \sum_{\mathbf{q}\nu} \sqrt{\frac{\hbar}{2m_{l\kappa}\omega_{\mathbf{q}\nu}}} \left(a_{\mathbf{q}\nu}\exp(-i\omega t) + a_{-\mathbf{q}\nu}^{\dagger}\exp(i\omega t) \right)$$
$$\exp\left[i\mathbf{q}\cdot\mathbf{R}_{l\kappa}^0\right](\hat{\mathbf{n}}_{l\kappa}^{\alpha}\cdot\mathbf{e}_{\mathbf{q}\nu}),$$

(4.15)

where $a^{\dagger}$ and a is the creation and annihilation operators [76]. The distribution of the atomic displacements can then be obtained as expectations values of Eq. (4.15). It can be shown [111] that the distribution is an uncorrelated multivariate Gaussian in *phonon* coordinates, or $\mathbf{q}$-space. The mean value is zero and the variance is given by the mean-squared displacement,

$$\langle(u_{l\kappa}^{\alpha})^2\rangle\,(T) = \frac{1}{N_q} \sum_{\mathbf{q}\nu} \frac{\hbar}{m_{l\kappa}\omega_{\mathbf{q}\nu}} \left[\frac{1}{2} + \langle n(\omega_{\mathbf{q}\nu}, T)\rangle\right] \left(|\hat{\mathbf{n}}_{l\kappa}^{\alpha}\cdot\mathbf{e}_{\mathbf{q}\nu}|\right)^2.$$

(4.16)

In the classical limit the mean-squared displacement becomes proportional to temperature,

$$\langle(u_{l\kappa}^{\alpha})^2\rangle\,(T\to\infty) = \frac{1}{N_q} \sum_{\mathbf{q}\nu} \frac{k_B T}{m_{l\kappa}\omega_{\mathbf{q}\nu}^2} \left(|\hat{\mathbf{n}}_{l\kappa}^{\alpha}\cdot\mathbf{e}_{\mathbf{q}\nu}|\right)^2,$$

(4.17)

while at low temperatures it approaches the zero-point motion value

$$\langle(u_{l\kappa}^{\alpha})^2\rangle\,(T=0) = \frac{1}{N_q} \sum_{\mathbf{q}\nu} \frac{\hbar}{2m_{l\kappa}\omega_{\mathbf{q}\nu}} \left(|\hat{\mathbf{n}}_{l\kappa}^{\alpha}\cdot\mathbf{e}_{\mathbf{q}\nu}|\right)^2.$$

(4.18)

The motion of a given phonon mode is given by its phonon displacement operator,

$$A_{q\nu}(t) = a_{\mathbf{q}\nu}\exp(-i\omega_{\mathbf{q}\nu}t) + a^{\dagger}_{-\mathbf{q}\nu}\exp(i\omega_{\mathbf{q}\nu}t).$$

The time correlation of this operator can be viewed as 'a propagating displacement wave' [112], and gives the expected harmonic motion,

$$\langle A_{\mathbf{q}\nu}(t)A^{\dagger}_{\mathbf{q}\nu}(0)\rangle = \exp(-i\omega_{\mathbf{q}\nu}t)(n_{\mathbf{q}\nu}+1) + \exp(i\omega_{\mathbf{q}\nu}t)n_{\mathbf{q}\nu}. \qquad (4.19)$$

Despite this propagator not being exactly the phonon propagator, we will adopt the same nomenclature as other Authors have [113–115] and to refer to this as the 'one-phonon imaginary-time Green's function', ignore that it is slightly misleading for the uninitiated. Time-correlations and their significance will be discussed more in detail in Chapter 5.

4.3   Sampling configurational space

When extracting the FCs one can make use of the frozen phonon method and displace one atom at the time. However, here we will consider the more efficient method and directly displace all atoms in the cell and thereby collecting training structures for the regression problem in Eq. (4.6). For instance, one can displace all atoms according to a normal distribution given some appropriate standard deviation. This method has been denoted Rattle [106].

A more proper, but also more computationally demanding way of generating the training structures, is to generate displacements using MD, preferably ab-initio molecular dynamics (AIMD).

Another attractive way to generate training structures is to make use of the derived normal modes. The normal modes can be populated according to some given temperature. To generate the atomic displacements, which are Gaussian distributed, the Box-Muller method can be used. The displacements are then given by

$$u_i^{\alpha} = \sum_{\nu} A_{\nu}^i e_{\nu}^{i,\alpha} \sqrt{-2\ln(Q_{\nu})} \cos(\pi U_{\nu}), \qquad (4.20)$$

where Q_{ν} and U_{ν} are two uniform random numbers between 0 and 1, and

$$A_{\nu}^i = \left[\frac{\hbar}{m_i\omega_{\nu}}\left(\frac{1}{2} + n(\omega_{\nu}, T)\right)\right]^{1/2}. \qquad (4.21)$$

We have here dropped the index $\mathbf{q}$, since we are only interested in the modes that are commensurate with the supercell, i.e., the modes at the Γ-point of the supercell. If we
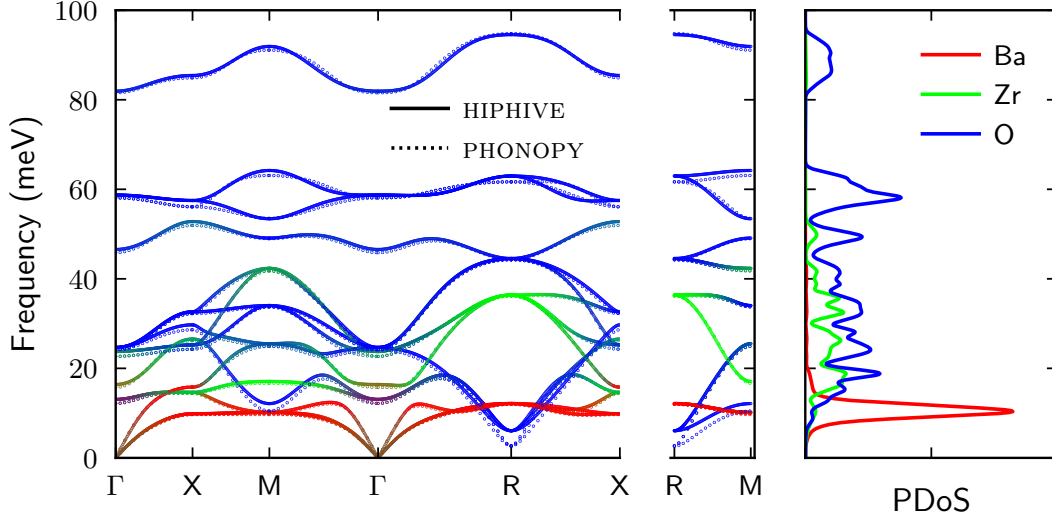
Figure 4.3: projected dispersion at the high symmetry points using HIPHIVE and PHONOPY in the $4 \times 4 \times 4$ supercell. Color assigned as (Ba, Zr, O) = (R, G, B).

would like to populate the modes classically instead, the amplitude

$$A_\nu^i = \left[\frac{k_B T}{m_i \omega_\nu^2} \right]^{1/2} \tag{4.22}$$

should be used.

In Fig. 4.3 we show results for BZO using the "standard" method based on individual atomic displacements with size 0.01 Å (here denoted PHONOPY) and using the method based on training structures and regression (here denoted HIPHIVE). The PHONOPY results are the same as in Fig. 4.1 and the HIPHIVE results are based on training structures from phonon modes at 100 K using the classical amplitude in Eq. (4.22). Both results are based on a 4x4x4 supercell and in the HIPHIVE calculations the cutoff for the FCs is set to 8.0 Å, about $L/2$, where $L = 4a_0 = 16.94$ Å is the supercell size. In the same figure we show the projected DoS which is smeared using a Gaussian kernel with $\sigma = 0.2$ meV.

We notice that the two methods give very similar results. There is, however, a difference for the lowest mode at the R point. That motion is strongly anharmonic, leading to a *renormalized* larger frequency for the HIPHIVE method. This is owing to the larger and more physical displacements that are sampled by that method.

4.4 Anharmonicity

The harmonic model provided equations for calculating frequencies, and, e.g., free energies. However, there are a lot of properties of a material that are related to the lattice that are not described by the harmonic approximation. For example, lattice thermal conductivity, thermal expansion, phonon lifetimes, soft modes and structural phase transitions [105, 116, 117]. Higher order terms from the expansion in Eq. (4.3), then have to be included. Keeping terms up to fourth order gives us,

$$ V = \frac{1}{2!}\Phi_{ij}^{\alpha\beta} u_i^\alpha u_j^\beta + \frac{1}{3!}\Phi_{ijk}^{\alpha\beta\gamma} u_i^\alpha u_j^\beta u_k^\gamma + \frac{1}{4!}\Phi_{ijkl}^{\alpha\beta\gamma\upsilon} u_i^\alpha u_j^\beta u_k^\gamma u_l^\upsilon. \tag{4.23} $$

It is apparent that we need methods that also address the anharmonic interactions.

4.4.1 Perturbation theory

The dynamics of the anharmonic system can be investigated by, e.g., perturbation theory. This is carried out by writing the harmonic Hamiltonian on a diagonal form using the creation and annihilation operators [116],

$$ \mathcal{H} = \sum_\lambda \hbar\omega_\lambda \left(a_\lambda^\dagger a_\lambda + \frac{1}{2} \right), \tag{4.24} $$

with energy eigenstates, $|n\rangle$, sometimes referred to as Fock states. The displacement operator, defined Eq. (4.15), was used to rewrite the Hamiltonian and $\lambda = (\mathbf{q}, \nu)$. A potential of the third order can then be written as [116],

$$ \mathcal{H}_3 = \sum_{\lambda\lambda'\lambda''} \Psi_{\lambda\lambda'\lambda''}(a_\lambda + a_{-\lambda}^\dagger)(a_{\lambda'} + a_{-\lambda'}^\dagger)(a_{\lambda''} + a_{-\lambda''}^\dagger), \tag{4.25} $$

where the same displacement operator is used and $-\lambda = (-\mathbf{q}, \nu)$. Extension to even higher orders is straight forward. The potential in Eq. (4.25) will cause scattering between the Fock states as, $\mathcal{H}_3$ contains terms such as, $a_\lambda^\dagger a_{\lambda'} a_{\lambda''}^\dagger$. As a result, the Fock states are no longer energy eigenstates of the Hamiltonian. One way to handle this issue is to use perturbation theory, given that the anharmonicity is weak.

Maradudin and Fien [118] have an excellent discussion on how the anharmonic system impacts the frequency of the system. They showed that the unperturbed system, the harmonic system, will experience a complex shift of the frequency, $\Delta\omega + i\Gamma$. The imaginary part (Γ) is related to the lifetime of the phonons, which leads to a broadening of the vibrational spectrum, which we will see later. The $\Delta\omega$ is simply a shift of the frequency. Ref. [116] uses perturbation theory to calculate Γ using a third order potential for a couple of different materials.

4.4.2 Quasi harmonic approximation

The simplest correction to the real part of the complex shift is due to the increased (or decreased) separation of the atoms at elevated temperatures, thermal expansion. The thermal expansion can be calculated directly from higher order derivatives of the potential energy surface as presented in [118], or by explicitly changing the volume and calculate a new set of frequencies, which is done in the quasi harmonic approximation [105]. Practically, this carried out by calculating the harmonic frequencies and electronic energies at a few different volumes, and then minimizing the free energy with respect to the volume at different temperatures. It is evident that the electronic energies increase with either an increase or decrease in volume. However, the frequencies are commonly decreasing with increasing volume as the bonds tends to soften. This increases the vibrational entropy, and in turn decreases the free energy, which leads to an expansion of the volume. It is worth noting that there exists materials with negative thermal expansion, but they are rare, see, e.g., [119].

4.4.3 Soft modes and structural phase transitions

As noted in the beginning of this chapter, it is not given that the potential was expanded around a minimum, it could as easily have been expanded around a saddle point (or a local maximum). That is, we know that the Jacobian is zero, however, for a minimum it is required that the Hessian matrix should be positive definite, that is, all eigenvalues are positive. Therefore, if the dynamical matrix, Eq. (4.7), which is related to the Hessian, exhibits negative eigenvalues we can conclude that the potential was not expanded around a minimum but rather at a saddle point. This means that the potential energy is lowered along the normal mode corresponding to that eigenvalue.

Structures that exhibit negative eigenvalues of the dynamical matrix are sometimes referred to as a *dynamically unstable* structure. However, at elevated temperatures, experiments might indicate that the *dynamically unstable* structure is the one that is observed. For example, $BaCeO_3$ undergoes a series of phase transitions from orthorhombic to rhombohedral to cubic. However, the dynamical matrix of the cubic and rhombohedral structure exhibits negative eigenvalues (imaginary frequencies) [120]. The explanation is that the anharmonic forces can stabilize the structure. Moreover, if the anharmonic interactions are very strong, the real part of the complex shift for the frequency might be large. Modes with large shifts of the frequency with respect to, e.g., the temperature, are sometimes referred to as soft modes.

4.5 Effective harmonic modelling

The idea behind effective harmonic modelling is to generate a harmonic model that best represents the anharmonic system at a specific temperature and, if needed, volume.

We will restrict the analysis to the temperature dependence, but extensions to include the thermal expansion is straight forward, although more computationally demanding. There exist a plethora of methods that implements this, see, e.g., [113, 121–124]. For example, some methods include the following minimization problem,

$$\min_{\mathbf{\Phi}(T)} \left\{ \langle (\mathscr{H} - \mathbf{\Phi}(T))^2 \rangle_\lambda \right\} . \tag{4.26}$$

$\mathbf{\Phi}(T)$ is the second order FC at temperature T and λ is the ensemble in which the minimization is carried out. While other methods rely on Green's functions [113, 124] or a variation formulation [121]. The ensemble can either be the harmonic ensemble which is generated by the model, or the anharmonic ensemble. The minimization is usually done with respect to the forces,

$$\min_{\mathbf{\Phi}} \left\{ \sum_{i\alpha} \left(F_i^\alpha - \Phi_{ij}^{\alpha\beta} u_j^\beta \right)^2 \right\} , \tag{4.27}$$

but the energy can easily be used/included if needed.

4.5.1 Temperature dependent effective potential

Hellman [123, 125] developed the temperature-dependent effective potential (TDEP) software package. This software package is based on a method that minimizes the difference between the harmonic model and the anharmonic system that we want to study, in the ensemble of the anharmonic system. This means that the samples, or snapshots, used in Eq. (4.27) can be, e.g., drawn from MD simulations. The minimization problem is then solved by casting the problem into a linear system of equations as discussed in Sect. 4.1 and the same methodology is employed here. A caveat of the method is that the snapshots have to be drawn sufficiently separated in time. Too frequent draws will lead to large correlations in the data, which is detrimental to the stability of the minimization problem. Other approaches based on MD simulation exists as well, see, e.g., [124]. Typically, the MD simulations are carried out by AIMD, although, other methods can in principle be used too.

A drawback of the method is that MD simulations are classical, i.e., we have forfeited the fact that the motion of the ions should be treated quantum mechanically. However, at higher temperatures, at least above the Debye temperature, the classical treatment should be valid.

4.5.2 Self consistent phonons

Contrary to the TDEP method the self consistent phonon (SCP) method minimizes the difference between the anharmonic system and the harmonic model in the ensemble
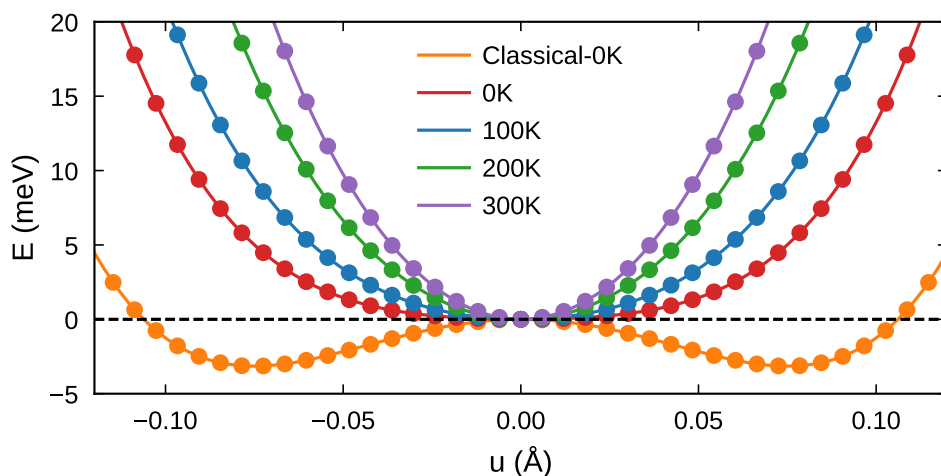
Figure 4.4: Temperature dependence of the tilt mode in BZO. The temperature dependence is from other thermally activated modes. The underlying functional used to generate the fourth order FC potential is PBEsol.

of the harmonic system. This means that, instead of MD simulations, the harmonic model is used to generate the snapshots with Eq. (4.20) for the minimization problem Eq. (4.27). The benefit of generating snapshots this way is that uncorrelated snapshots are easily generated. However, the drawback is that we need to solve the minimization problem self-consistently. Say, e.g., that your initial guess of the effective harmonic model (EHM) at the finite temperature T is generated with the frozen phonon method. The new model that minimizes Eq. (4.27) for the generated snapshots will be different from the initial model. Therefore, the snapshots generated from this model will be different as well. This procedure of generating snapshots and solving the minimization problem will continue until the difference between the model used to generate the snapshot and the model that solves the minimization problem has converged. There exist a few different methods that fall under the SCP name, see e.g., Refs. [113, 121, 122].

It is worth noting that contrary to the TDEP method, it is trivial to incorporate quantum effects in the SCP method as Eq. (4.20) with Eq. (4.21) is quantum mechanical. The effect of the quantum statistics is that, e.g., the zero point energy leads to a non-zero displacement at T=0 K and, in effect, a larger frequency, than what is probed by, e.g., TDEP at low temperatures.

In Fig. 4.4 we show the stabilization of the potential landscape of the AFD mode in BZO at T=0 K as a consequence of these quantum effects. First, note that the energy decreases along the specific mode if all other phonon modes are frozen, this is marked as Classical-0K in the figure. However, a temperature can be modelled by occupying all other modes except the AFD mode at a specific temperature using Eq. (4.20) for the EHM constructed at that specific temperature. The potential is then mapped along the

mode with different amplitudes (unrelated to the temperature). The potential energy is then averaged over a large set of thermally activated structure. We then set the average potential energy to zero for the structures with zero amplitude. From the potential landscape, one can conclude that the zero point motion stabilizes the structure. In this case, the interpretation is that structure is unable to localize in the potential minimum, even at T=0 K. However, the validity of the phonon quasi-particle close to a phase transition is poorly understood, and one should therefore be cautious of this conclusion. Nevertheless, one thing is certain, the potential stiffens as the temperature is increased due to the other phonon modes.

4.5.3 Discussion

As previously noted, the essential difference between TDEP and SCP is in what ensemble we carry out the minimization and that it is trivial to include quantum statistics in the SCP method. However, due to the non-interactive approximation of the phonons, it is likely that the SCP probes higher energy parts of phase space. Nevertheless, we are trying to create an effective second order potential, not reproduce the fully anharmonic system. It is therefore not obvious which of these methods produces the best model.

Metsanurk *et al.* [126] used thermodynamic integration to discuss the errors involved in accounting for anharmonic effects in this way. The thermodynamic integration was set up such that a few values of λ were tested in between the anharmonic and harmonic Hamiltonian. They argue that, errors in the free energy of the EHMs is due to the lack of transferability. The EHMs manages to describe the average potential energy in the ensemble which it was trained in. However, it fails to extrapolating to a general λ value and therefore fails to correctly describe the actual anharmonic energies. They found that TDEP consistently underestimated, whereas SCP consistently overestimated the average potential energy for all values of λ.

We tested both TDEP and SCP to study the AFD mode in BZO with a FCP based on PBE. The frequency from TDEP is slightly lower than the frequency from SCP. A likely explanation for the higher frequencies in SCP is due to the on average larger potential energy compared to the average potential energy in TDEP.

Fig. 4.5 shows the calculated frequencies as a function of temperature for the two methods. SCP-cl is the classical version of SCP, meaning that the classical amplitude ($\hbar\omega << k_B T$) has been used in Eq. (4.20). SCP-qm and SCP-cl are almost completely equal at and after 100 K, however, below that temperature there is a significant difference between the two. This demonstrates the importance of accounting for the quantum motion at low temperatures.
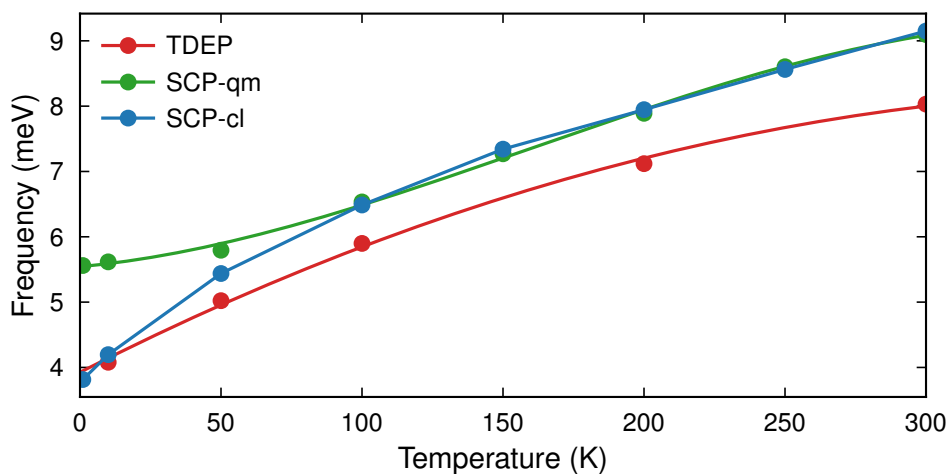
Figure 4.5: Temperature dependence of the frequency of the tilt mode in BZO using a FCP based on PBE. SCP-cl uses the classical limit for the amplitude of the phonon, while SCP-qm uses the correct quantum amplitude.

4.6 Higher order models and inter-atomic potentials

By making use of the Taylor series expansion in Eq. (4.3), we can construct an inter-atomic potential with a suitable truncation of the series expansion. That is, we can fit a potential to interpolate the DFT results. However, it is important to note that the Taylor series breaks down for large displacements and is not well-defined when atoms start to diffuse, or when the system lacks equilibrium positions, such as liquids. Therefore, considerable effort has been devoted to derive more general and generic inter-atomic potentials based on some modelling of the potential energy function $V(\dots, \mathbf{R}_i, \dots)$, Eq. (4.1). There exist a vast number of such potentials such as, e.g., the embedded atom method (EAM), bond order potentials or Lennard-Jones potential. These potentials are inspired from physical insights, setup, as to mimic certain known features of the atomic interactions. ATOMICREX [127], is a software that provides a framework to construct these type of potentials. The potentials is not restricted to modelling of crystals and does not break down for large displacements or diffusing atoms, however, they have very limited accuracy. Therefore, in more recent times, Behler *et al.* used neural networks [128] and Jinnouchi *et al.* active learning [129] to model the potential energy. Notably, there has been an explosion of these types of models, see, e.g., Refs. [130–134] These methods do not use the series expansion, but instead a set of chemical descriptors [135]. Moreover, they do not rely on physical intuition, and can therefore be engineered to have a more flexible form, allowing them to better describe the interatomic interactions

at the cost of being more difficult to fit. These models can, e.g., be used to substitute the much more expensive option of, e.g., DFT in, MD. This reduces the computational demand significantly, and it is possible to extract thermodynamic [136–138] and dynamical properties [139] with near DFT accuracy a lot cheaper.

As we have previously mentioned, the limitation of MD is that the motion is treated classically. Therefore, below some temperature, usually assumed to be the Debye temperature, it is questionable to run MD simulations. Below this temperature, the path integral formulation should be used to calculate, e.g., free energies and static properties, such as the static structure factor. However, dynamical properties can only be approximated with the path integral formulation. A slurry of different methods have been developed based on the path integral formulation, however, the simplest method is probably the centroid molecular dynamics. This method appears to give an approximate solution of dynamical properties [140, 141]. For example, Ref. [142] uses the path integral formulation and centroid molecular dynamics to study dynamical and static properties of quartz, and compares it to the classical dynamics. The use case for inter-atomic potentials is crystal clear here, the combination of the path integral formulation with AIMD is very computationally demanding, and a significantly faster potential is preferable, or may even be necessary.

5

Time correlations and spectra

Time correlation functions describe the dynamics of a system, and are strongly linked to scattering experiments. The derivation of the correlation functions is based on Fermi's golden rule and a perturbing potential, V_{pert}, which describes the weak interaction between the probe and the sample. For time-independent potentials this is given by,

$$P_{i \rightarrow f} = \frac{2\pi}{\hbar} |\langle f|V_{\mathrm{pert}}|i\rangle|^2 \delta(E_f - E_i), \qquad (5.1)$$

where i is the initial state and f the final state, both the initial and final state include the probes incoming and outgoing state. It turns out that, when considering the occupation of the initial states, and summing over both initial and final states, Fermi's golden rule turns into a time correlation function, see, e.g., Refs. [143, 144].

5.1 Scattering with neutrons

The intermediate scattering function is an example of an important time correlation function, and we will see that this time correlation function depends directly on the atomic positions, which makes the connection between theory and experiments direct.

The perturbing potential that couples the sample and the neutrons is commonly assumed to be on the form of a Fermi pseudo-potential,

$$V_{\mathrm{pert}} = \frac{2\pi\hbar}{M_n} b\delta(\boldsymbol{r} - \boldsymbol{R})$$

where M_n is the mass of the neutron, $\boldsymbol{R}$ and $\boldsymbol{r}$ is the coordinate of a given scattering atom and the impinging neutron, and b is the scattering length, which depends on the scattering atom. From this potential and Fermi's golden rule, Eq. (5.1), the differential

cross-section can be derived. When correctly accounting for the kinematics of the neutrons, this is given by [144],

$$\left(\frac{d^2\sigma}{d\omega_f d\Omega}\right) = b^2 \frac{k_f}{k_i} S(\boldsymbol{q}, \omega) \tag{5.2}$$

where $\boldsymbol{k}_f$ and $\boldsymbol{k}_i$ is the wave vector of the scattered and incoming neutron, $\mathbf{q} = \mathbf{k}_i - \mathbf{k}_f$, and $S(\boldsymbol{q}, \omega)$ is the dynamical structure factor, where ω is the frequency shift of the neutron. The dynamical structure factor is given as the temporal Fourier transform of the intermediate scattering function,

$$S(\mathbf{q}, \omega) = \int_{-\infty}^{\infty} dt \, \exp(-i\omega t) F(\mathbf{q}, t), \tag{5.3}$$

where the intermediate scattering function is given as,

$$F(\mathbf{q}, t) = \frac{1}{N} \langle n(\mathbf{q}, t) n(-\mathbf{q}, 0) \rangle. \tag{5.4}$$

Here, $n(\mathbf{q}, t)$ is the spatially Fourier transformed atomic density,

$$\begin{aligned} n(\mathbf{q}, t) &= \int d\mathbf{r} \sum_i \delta(\mathbf{r} - \mathbf{R}_i(t)) \exp\left(i\mathbf{q} \cdot \mathbf{r}\right) \\ &= \sum_i \exp\left(i\mathbf{q} \cdot \mathbf{R}_i(t)\right). \end{aligned} \tag{5.5}$$

For multi-component systems, the intermediate scattering function will be decomposed into partial intermediate scattering functions (where the scattering length can be included),

$$F_{AB}(\mathbf{q}, t) = \frac{b_A b_B}{\sqrt{N_A N_B}} \langle n_A(\mathbf{q}, t) n_B(-\mathbf{q}, 0) \rangle.$$

The intermediate scattering function is then given as a sum over all partial intermediate scattering functions.

To see the connection between neutron scattering and the phonons calculated in Chapter 4, one has to approximate the intermediate scattering function, Eq. (5.4). This process is quite involved, but excellently explained in [118] and will thus not be repeated in detail here. However, in short, this involves a cumulant expansion of the intermediate scattering function and a subsequent Taylor expansion of the cumulant expansion. This leads to an expression that is proportional to the one-phonon imaginary-time Green's functions.

5.1.1 Harmonic approximation

In the harmonic approximation, the one-phonon imaginary-time Green's functions is a purely oscillating function with an infinite lifetime and a frequency given by the corresponding phonon, see Eq. (4.19). Thus, for a single phonon excitation or de-excitation, i.e., stokes and anti-strokes scattering, the coherent dynamical structure factor Eq. (5.3) is given as [145],

$$S(\mathbf{q}, \omega) = \exp(-2W) \sum_{\nu} \Big(|F(\mathbf{q}, (-\mathbf{k})\nu)|^2 (1 + n_{\mathbf{k}\nu}) \delta(\omega - \omega_{\mathbf{k}\nu}) + $$

$$|F(\mathbf{q}, \mathbf{k}\nu)|^2 n_{\mathbf{k}\nu} \delta(\omega + \omega_{\mathbf{k}\nu}) \Big), \tag{5.6}$$

with

$$F(\mathbf{q}, \mathbf{k}\nu) = \sum_{\kappa} \sqrt{\frac{\hbar}{2M_{\kappa}\omega_{\mathbf{q}\nu}}} \exp\left(i(\mathbf{q} + \mathbf{k}) \cdot \mathbf{R}_{\kappa}^0\right) \left(\mathbf{q} \cdot \mathbf{e}_{\mathbf{q}\nu}^{\kappa}\right),$$

where $\mathbf{k}$ is a vector within the first Brillouin zone that is chosen such that $\mathbf{q} - \mathbf{k} = \mathbf{G}$ for the first term and $\mathbf{q} + \mathbf{k} = \mathbf{G}$ for the second term, where $\mathbf{G}$ is a reciprocal lattice vector. The prefactor, $\exp(-2W)$, is the Debye-Waller factor [145], which is related to the mean squared displacement. Moreover, in this approximation, we note that the shape of the peak is a delta function and for some phonon modes this can be in stark contrast to the measured experimental lineshape, which can have a more complicated shape. This more complicated shape is a consequence of the anharmoncity, the interaction between the phonon modes shifts and broadens the peaks, which was briefly discussed in Chapter 4.

Two, three, and even higher order phonon processes can also be calculated using the harmonic approximation. For a two phonon process, the peaks will be localized at $\omega_1 + \omega_2$, $\omega_1 - \omega_2$, $\omega_2 - \omega_1$ and $-(\omega_1 + \omega_2)$. However, other processes exist as well, but they can only be non-zero for anharmonic systems and usually only contributes a background.

5.1.2 Anharmonicity

Clearly, the harmonic approximation is a simplification of real systems which are anharmonic. Fortunately, it is possible to go beyond the harmonic approximation by approximating the one-phonon imaginary-time Green's functions, including anharmonicity. This can be carried out via perturbation theory, see, e.g., [116], or more commonly via the diagrammatic approach, which is outlined in Ref. [118]. They summarized the diagrammatic method with the memorable sentence (with some adaptation): a free phonon enters at time $t = 0$, "Things of arbitrary complexity happen", and another free phonon emerges at time $t = \tau$. The one-phonon imaginary-time Green's function is then calculated by including the most probable interactions that can happen in
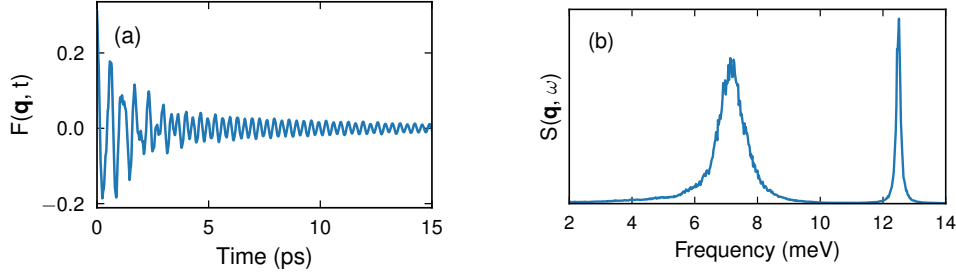
Figure 5.1: Result for a FCP constructed with PBE for BZO at T=200 K. (a) Intermediate scattering function and (b) Dynamical structure factor.

between those two times, the interactions are depicted as diagrams (hence the name). The benefit of the diagrammatic approach is that quantum statistics can be included, however, including all anharmonicity and all interactions are not possible, i.e., we have to truncate the expansion at some point.

Approximations of the one-phonon imaginary-time propagator can also be found by using, e.g., mode projection schemes [146–148] or from EHMs, see Sect. 4.5, however, the EHMs only models the frequency shift and ignores the broadening of the peak.

5.1.3 Sampling

The intermediate scattering function can be directly evaluated from MD. This includes all possible interactions but are limited to classical statistics, in contrast to the diagrammatic approach.

We utilized this method in **PAPER I** to calculate the intermediate scattering function and the resulting dynamical structure factor (with $b_{Ba} = b_{Zr} = b_O = 1$) for BZO using a FCP constructed with PBE at, $\mathbf{q} = (2\pi/a_0)(2.5, 0.5, 0.5)$ and T=200 K using MD. The individual peaks in the spectrum can be fitted to the functional form derived from a damped harmonic oscillator [139],

$$f(\omega) = A \frac{2\Gamma\omega_0^2}{\left(\omega^2 - \omega_0^2\right)^2 + (\Gamma\omega)^2},$$

where Γ is related to the oscillator lifetime and ω_0 is the undamped frequency. Examining the intermediate scattering function, Fig. 5.1, we can clearly see an oscillator with a large amplitude that is heavily damped, i.e., it decays quickly in time. This corresponds to the broader peak at about ~ 7 meV seen in the dynamical structure factor. There is also a higher frequency component visible with smaller amplitude and lower damping. This corresponds to the more narrow peak at ~ 12.5 meV.

However, we must note that the self-energy, which is the complex shift of the frequency briefly mention in Sect. 4.4, can have a complicated frequency dependence as

described in [146], then, this fit to a damped harmonic oscillator is unreasonable. For example, a single oscillator can have a complicated double peak shape, sometimes referred to as a satellite, which has been found in, e.g., PbTe [149–151].

5.2 IR scattering

Another useful correlation function is that of the total dipole moment, which shall be apparent in the following section. The total dipole moment depends indirectly on the positions of the atoms, i.e., a secondary calculation is needed. This makes the comparison between theory and experiments less direct than, e.g., neutron scattering. On the flip side, IR experiments are much easier to carry out than neutron scattering, and it is therefore preferable from an experimental point of view, with some caveats. For example, all phonon modes are not directly visible in the spectrum.

It turns out that, using the dipole approximation [143], the perturbing potential that couples the electrical field to the sample is given as,

$$V_{\text{pert}} = \boldsymbol{\mu} \boldsymbol{E} = \Omega_0 \boldsymbol{P} \cdot \boldsymbol{E}, \tag{5.7}$$

where $\boldsymbol{\mu}$ is the (total) dipole, Ω_0 the volume of the unit cell, $\boldsymbol{P}$ the polarization and $\boldsymbol{E}$ the electrical field. From now on, we will stick with the polarization as the dipole is typically only used for molecules, and we are studying crystals where the nomenclature of polarization is more common. From this perturbing potential, we can derive the absorption cross-section for IR spectroscopy by once again using Fermi's golden rule, and by assuming that the presence of the electrical field does not change the dynamics of the system. This means that we do not account for any induced polarization due to the presence of the electrical field.

5.2.1 Polarization

The polarization can, e.g., be due to intrinsic properties of the molecule or material. For example, water and ferroelectric materials have a permanent polarization even in the absence of an electrical field. However, crystals or molecules without permanent polarization can still have an instantaneous polarization due to, e.g., minute displacement of the atoms from its ideal positions, i.e., due to vibrations.

The polarization is naively defined as,

$$\boldsymbol{P} = \frac{1}{\Omega_0} \int_{\text{sample}} \boldsymbol{r} \rho(\boldsymbol{r}) \mathrm{d}\boldsymbol{r}.$$

However, in a periodic system, this is not well-defined, as described by Resta and Vanderbilt in the phenomenal work of Modern theory of polarization [152]. On a positive

41

note, though, this problem was also solved in the same work. The solution is that the polarization can be written as,

$$P = \frac{1}{\Omega_0} \left(\sum_i Q_i R_i + \sum_{n=\text{occ}} \langle W_n | \mathbf{r} | W_n \rangle \right) \tag{5.8}$$

where W_n is the Wannier function of the n-th occupied orbital, R_i is the position of the i-th ion core, Q_i and r is the position operator for the electrons. Still, the total polarization does not make sense on its own, this is because of something referred to as the polarization quantum. That is, the polarization is only well-defined modulo $f|e|\mathbf{R}/V_0$ for the electronic system, where $\mathbf{R}$ is a lattice vector. Equivalent problems exist for the ionic system. However, changes in polarization are well-defined as long as you stay on the same "branch" of the polarization quantum, see, e.g., Refs. [152, 153].

5.2.2 IR absorption cross-section

Assuming that the frequency of the light is close to the frequencies of the vibrations of the system means that we can completely ignore the electronic system. Under these circumstances, when the light source is that of a monochromatic light, the perturbing potential is given by,

$$V_{\text{pert}} = E_0 \mathbf{P} \cdot \hat{\varepsilon} \cos \omega t,$$

where E_0 is the field strength and $\hat{\varepsilon}$ is the direction of the field. Following [143], the derivation of the IR absorption is then given as the rate of energy loss from the radiation to the system. This can be calculated via Fermi's golden rule, Eq. (5.1), which leads to the absorption cross-section,

$$\alpha(\omega) = \frac{4\pi^2}{\hbar c n} \omega \left(1 - \exp(-\beta\omega) \right) M(\omega). \tag{5.9}$$

where c is the speed of light, n the refractive index of the sample and $M(\omega)$ is the IR absorption lineshape which is given by the Fourier transform of the polarization time correlation function,

$$M(\omega) = \frac{1}{2\pi} \int_{-\infty}^{\infty} \langle (\varepsilon \cdot \mathbf{P}(t)) \left(\varepsilon \cdot \mathbf{P}^\dagger(t+\tau) \right) \rangle e^{-i\omega\tau}. \tag{5.10}$$

5.3 Raman scattering

Similarly to IR scattering, Raman depends indirectly on the position of the atoms. However, in this case, the important property is the dielectric susceptibility. Once again, we will use Fermi's golden rule to derive the cross-section. However, note that Fermi's

golden rule is derived by using first order perturbation theory, but Raman is not a first order process, as this requires knowledge of interactions between the electrons with the photon field and the interaction between the ionic system with the electronic system. The polarization, Eq. (5.8), as discussed above, is used to abstract away the electronic system, which means that we can make use of first order perturbation theory. The perturbing potential in the case of Raman is still given by the dipole approximation. However, in this case, we are interested in the induced polarization due to the presence of the electrical field.

5.3.1 Dielectric susceptibility

The induced polarization caused by an external electrical field $\mathbf{E}$, is related to the dielectric susceptibility χ, by,

$$\boldsymbol{P}_{\text{ind}} = \chi(\omega)\mathbf{E}, \tag{5.11}$$

where $\boldsymbol{P}_{\text{ind}}$ is the induced polarization. Due to the different time scales of the electrons and ions, one of the subsystems will dominate for a given frequency of the light. This means that the dielectric susceptibility can be decomposed into an ionic and an electronic part,

$$\chi = \chi_{\text{ion}}(\omega) + \chi_{\text{el}}(\omega). \tag{5.12}$$

note that the dielectric susceptibility is frequency dependent, however, we will deal with the static ion clamped limit [154, 155], which is frequency independent. This approximation is valid in the frequency region between ionic and electronic absorption/resonance. This means that we will drop the frequency dependence and only deal with the electronic part, as this will be the dominate contribution in this frequency region. This is due to the slower dynamics of the ionic system, i.e., it can't effectively screen the electrical field.

Furthermore, we note that for linear optics, which is considered here, the components of the dielectric susceptibility are given as

$$\chi_{ij} = \frac{d\text{P}_i}{d\text{E}_j},$$

which can, e.g., be calculated with finite differences. A more common approach, however, is to connect the dielectric susceptibility to a density response [155]. The evaluation of the dielectric susceptibility is then carried out via a berry phase calculation [152].

Now using Eq. (5.11) in Eq. (5.7) we find that,

$$V_{\text{pert}} = \Omega_0 E_0 \hat{\boldsymbol{\varepsilon}}^{\text{out}} \cdot \left(\chi_{\text{el}} \cdot \hat{\boldsymbol{\varepsilon}}^{\text{in}} \right).$$

Hence, using classical electrodynamics we can interpret this as, the initially incoming photon polarizes the sample, the outgoing (or scattered) photon is created as radiation of the induced oscillating polarization.

5.3.2 Raman cross-section

Similarly to the IR-absorption, the differential-cross section for the Raman intensity can be derived using Fermi's golden rule Eq. (5.1). By correctly accounting for the kinematics of the radiating polarization, the differential cross-section is given as [156],

$$\left(\frac{d^2\sigma}{d\omega_{out}d\Omega}\right) = \left(\frac{\omega_{in} - \omega}{c}\right)^4 \sum_{\alpha\beta\gamma\delta} \hat{\varepsilon}_\alpha^{out} \hat{\varepsilon}_\beta^{out} L_{\alpha\gamma\beta\delta}(\omega) \hat{\varepsilon}_\gamma^{in} \hat{\varepsilon}_\delta^{in}, \qquad (5.13)$$

where c is the speed of light, Ω is a solid angle, ω_{in} and ω_{out} is the frequency of the incoming and outgoing light, respectively and $\omega = \omega_{in} - \omega_{out}$ is the frequency of the crystal excitation. $\hat{n}^{out}$ and $\hat{n}^{in}$ is the polarization of the outgoing and incoming light, respectively. Lastly, $L(\omega)$ is the Raman lineshape, which is given by,

$$L_{\alpha\gamma\beta\delta}(\omega) = \frac{1}{2\pi} \int_{-\infty}^{\infty} d\tau \, \langle \chi_{\alpha\gamma}^{\infty}(t) \chi_{\beta\delta}^{\infty\dagger}(t+\tau) \rangle \, e^{-i\omega\tau}. \qquad (5.14)$$

As can be seen in Eq. (5.13) the polarization of the incoming and scattered light picks out components of the dielectric susceptibility tensor. It is therefore important in experimental settings to keep track of the polarization.

The contribution from different elements of the Raman lineshape for a few different experimental setups in a cubic phase has then been tabulated by Cowley [157]. For a powder sample the Raman tensor has to be averaged instead, a formula for the intensity in this case has been given by McQuarrie [143].

Fig. 5.2 depict the polarized Raman spectrum of tetragonal BZO, where the elongated axis is along the z coordinate. In a), at $\theta = 0$, the incoming and outgoing light is along the x-axis, the crystal is then rotated around the z-axis, such that the incoming and outgoing light is instead polarized along the y-axis at $\theta = \pi/2$. This is referred to as parallel polarized Raman spectrum and is usually denoted in Porto notation as Z(XX)$\overline{Z}$. The letters outside the parenthesis denote the direction of the incoming and outgoing light (bar denotes the opposite direction), respectively, and the letters inside the parenthesis denotes the polarization of the incoming and outgoing light, respectively. For b), the setup is similar, however, in this case the outgoing light is instead rotated about 90° degrees from the incoming light. This is referred to as cross polarized Raman spectrum and is denoted in Porto notation as Z(XY)$\overline{Z}$. Note that some peaks are only visible during certain experimental setups.

Lastly, it is instructive to compare Eq. (5.13) and Eq. (5.9), which contrasts the difference in the meaning of the frequency between the Raman Eq. (5.14) and IR Eq. (5.10) experiments. In Raman, the frequency axis describes the frequency shift of the incoming light ($\omega_{in} - \omega_{out}$), whereas for IR, the frequency instead describes how much light the sample absorbs for that specific frequency of the excitation laser.
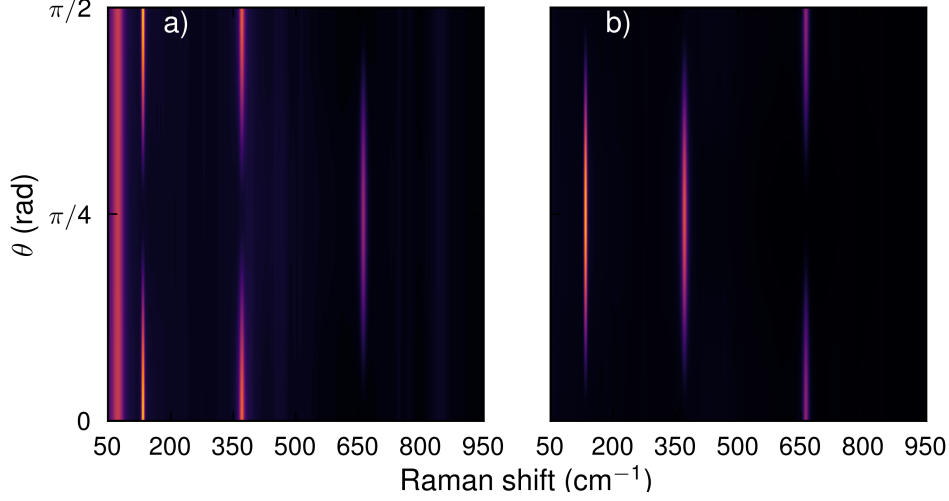
Figure 5.2: Polarized Raman spectrum of BZO for the tetragonal phase at P=18 GPa and T=300 K. a) Parallel polarized: the incoming and outgoing light is polarized along the $\hat{x}$-direction for $\theta = 0$ and the crystal is rotated about the z axis for larger angles. b) Cross polarized: the incoming light is polarized along the $\hat{x}$-direction and the outgoing is polarized along the $\hat{y}$-direction for $\theta = 0$ and the crystal is rotated about the z axis for larger angles.

5.4 Understanding Raman using phonons

The dielectric susceptibility, or equivalently the polarization, can be expanded in any collective coordinate of interest [158, 159]. This expansion can be used to analyze the Raman or IR spectrum. However, in this section, we will stick with the dielectric susceptibility as the polarization is completely analogous.

For example, to see the relation to the vibrational motion of the sample, we can expand the dielectric susceptibility in terms of phonon modes,

$$\chi = \chi_{\text{el}}^{(0)} + \sum_{\substack{q \\ \nu}} \mathscr{R}_{q}^{\nu} \tilde{u}_{q}^{\nu} + \frac{1}{2} \sum_{\substack{qk \\ \nu\mu}} \mathscr{R}_{q,k}^{\nu,\mu} \tilde{u}_{q}^{\nu} \tilde{u}_{k}^{\mu} + \dots \ . \tag{5.15}$$

where $\tilde{u}_{q}^{\nu}$ is the Fourier amplitude (phonon mode) given by the components of the sum in Eq. (4.15),

$$\tilde{u}_{q}^{\nu} = \left(\frac{\hbar}{2N_q \omega_{q}^{\nu}} \right)^{1/2} \left[a_{q}^{\nu} + a_{-q}^{\nu \dagger} \right],$$

and $\mathscr{R}$ is the Raman intensity for the respective order. The first order intensity is given

by, which is most easily identified by starting from a real space expansion,

$$
\begin{aligned}
\mathscr{R}_{\mathrm{q}}^{\nu} &= \sum_{l\kappa} \frac{\partial \chi_{\mathrm{el}}}{\partial u_{l\kappa}} \frac{e_{\mathrm{q}\nu}^{l\kappa}}{\sqrt{m_l}} \exp\left(i\mathbf{q} \cdot \mathbf{R}_{l\kappa}^0\right) \\
&= \sum_{l\kappa} \frac{\partial \chi_{\mathrm{el}}}{\partial u_{l\kappa}} \frac{e_{\mathrm{q}\nu}^{l\kappa}}{\sqrt{m_l}} \Delta_{\mathrm{q}},
\end{aligned}
\tag{5.16}
$$

where the last equality follows from momentum conservation, or more formally, due to the invariance of the crystal against rigid body translations. The higher order Raman intensities follows from similar calculations but with a wealth of more indices. These are still straight forward to derive, thus, the conservation rules that follows from the derivatives will not explicitly be derived but implicitly assumed.

One usually discusses the order of the Raman scattering based on how many phonon operators that are involved in the scattering event. For example, if one were to insert only the second term from Eq. (5.16) into the Raman lineshape Eq. (5.14), the correlation function would involve two phonon operators, which is referred to as first order Raman scattering. Inserting only the third term would instead give an expression involving four phonon operators, referred to as second order Raman scattering. However, one can also derive combinations of the first order and second order, which gives three phonon operators. These are uncommon to discuss and does not, to my knowledge at least, have and "order" associated with them. Nevertheless, Benshalom *et al.* [115] briefly discuss the impact of these terms and states that they will decay rapidly away from the first order peaks.

It is not uncommon to solely discuss Raman in terms of first order scattering. Therefore, it is important to know which modes that are first order active. Note that, from the definition of the first order intensity, Eq. (5.16), in order for the mode to be first order active, the dielectric susceptibility has to have a non-zero first order derivative with respect to the mode. Which mode that has a non-zero first order derivative can be derived from the symmetry of the crystal, see, e.g., [160]. Note that the cubic phase does not exhibit any first order Raman scattering due to its symmetry. It is therefore not uncommon to state that cubic crystals should lack a Raman spectrum.

Inserting the first order term from the Taylor expansion and the above definitions into the correlation function, Eq. (5.16), one finds that the first order Raman spectrum is given as,

$$
I_{\alpha\gamma\beta\delta}^{(1)}(\omega) = \frac{\lambda_s^4}{2\pi} \sum_{\nu\nu'} (\mathscr{R}_{\Gamma}^{\nu})_{\alpha\gamma} (\mathscr{R}_{\Gamma}^{\nu'})_{\beta\delta}^{\dagger} \tilde{G}_{\Gamma}^{\nu;\nu'}(\omega),
$$

where $\tilde{G}_{\Gamma}^{\nu;\nu'}(\omega)$ is proportional to the one-phonon imaginary-time Green's function given as,

$$
G_{\Gamma}^{\nu;\nu'}(t) = \langle u_{\Gamma\nu}(t) u_{\Gamma\nu'}^{\dagger}(0) \rangle \propto \langle A_{\Gamma\nu}(t) A_{\Gamma\nu'}^{\dagger}(0) \rangle .
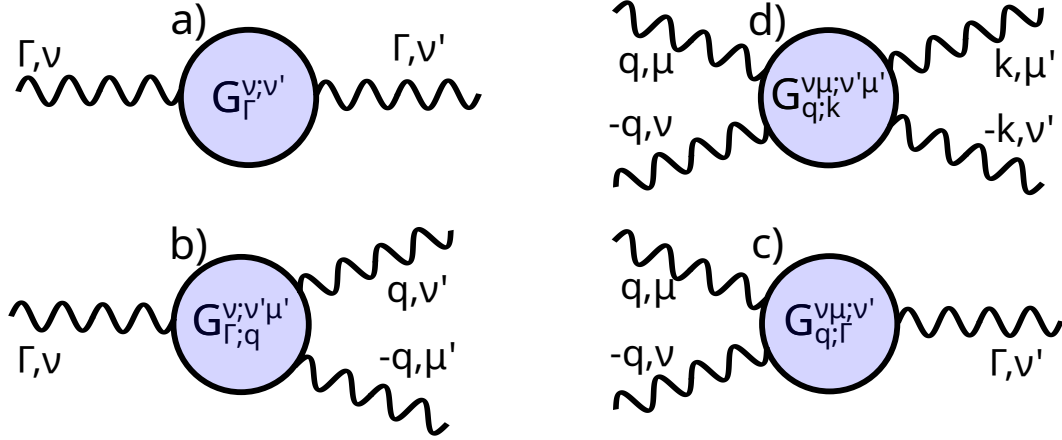\tag{5.17}
$$

Figure 5.3: Illustration of the Green's functions associated with Raman scattering. The blue circle indicates arbitrary interactions in between the two times $t = 0$ and $t = \tau$ and the G indicates which correlation the diagram is associated with. a) Shows first order Raman scattering, a free phonon $(\mathbf{\Gamma}, \nu)$ enters and at a later time another free phonon $(\mathbf{\Gamma}, \nu')$ leaves. b) Shows a mixed first and second order Raman scattering, a free phonon $(\mathbf{\Gamma}, \nu)$ enters and at a later time two free phonons $(\mathbf{q}, \nu'$ and $-\mathbf{q}, \mu')$ leaves. c) Same as b) but in reverse. d) Shows a second order Raman scattering, two free phonons $(\boldsymbol{q}, \nu, \textrm{-}\boldsymbol{q}, \mu)$ enters and at a later time two free phonons $(\mathbf{k}, \nu'$ and $-\mathbf{k}, \mu')$ leaves.

Combining the first with the second order expansion instead gives,

$$L^{(1/2)}_{\alpha\gamma\beta\delta}(\omega) = \frac{1}{4\pi} \sum_{\substack{\mathbf{q} \\ \nu\nu'\mu'}} (\tilde{\mathscr{R}}^{\nu}_{\mathbf{\Gamma}})_{\alpha\gamma} (\tilde{\mathscr{R}}^{\nu'\mu'}_{\mathbf{q};-\mathbf{q}})^{\dagger}_{\beta\delta} \tilde{G}^{\nu;\nu'\mu'}_{\mathbf{\Gamma};\mathbf{q}}(\omega) +$$

$$\frac{1}{4\pi} \sum_{\substack{\mathbf{q} \\ \nu\mu\nu'}} (\tilde{\mathscr{R}}^{\nu\mu}_{\mathbf{q};-\mathbf{q}})_{\alpha\gamma} (\tilde{\mathscr{R}}^{\nu'}_{\mathbf{\Gamma}})^{\dagger}_{\beta\delta} \tilde{G}^{\nu\mu;\nu'}_{\mathbf{q};\mathbf{\Gamma}}(\omega),$$

where the Green's functions associated with these terms are

$$G^{\nu\mu;\nu'}_{\mathbf{q};\mathbf{\Gamma}}(t) \propto \langle A_{\mathbf{q}\nu}(t) A_{-\mathbf{q}\mu}(t) A^{\dagger}_{\mathbf{\Gamma}\nu'}(0) \rangle$$

$$G^{\nu;\nu'\mu'}_{\mathbf{\Gamma};\mathbf{q}}(t) \propto \langle A_{\mathbf{\Gamma}\nu}(t) A^{\dagger}_{\mathbf{q}\nu'}(0) A^{\dagger}_{-\mathbf{q}\mu'}(0) \rangle. \tag{5.18}$$

Combining the second order expansion gives,

$$I^{(2)}_{ijkl}(\omega) = \frac{\lambda^4_s}{8\pi} \sum_{\substack{\boldsymbol{qk} \\ \nu\mu\nu'\mu'}} \left(\mathscr{R}^{\nu\mu}_{\mathbf{q};-\mathbf{q}}\right)_{\alpha\gamma} \left(\mathscr{R}^{\nu'\mu'}_{\mathbf{k};-\mathbf{k}}\right)^{\dagger}_{\beta\delta} \tilde{G}^{\nu\mu;\nu'\mu'}_{\mathbf{q};\mathbf{k}},(\omega). \tag{5.19}$$

where the two-phonon imaginary-time Green's function associated with this term is,

$$G_{\mathbf{q};\mathbf{k}}^{\nu\nu';\mu\mu'}(t) \propto \langle A_{\mathbf{q}\nu}(t)A_{-\mathbf{q}\mu}(t)A_{\mathbf{k}\nu'}^{\dagger}(0)A_{-\mathbf{k}\mu'}^{\dagger}(0)\rangle. \qquad (5.20)$$

The visualization of the Green's function stemming from the above terms is depicted in Fig. 5.3. The blue circles indicated that arbitrary scattering events takes place in between two times. That is, one or two phonons enters and one or two phonons emerges at a different time. These correlations functions can be evaluated directly from MD simulations by projecting on the phonons [146–148] or via the diagrammatic method which is also outlined in [115], for reference, see, [118].

It is also instructive to first study a purely harmonic system, where the following statements can easily be verified by utilizing Eq. (4.15). For a harmonic system, only specific parts of the expansion will contribute to the Raman spectrum. We first note that phonon modes are uncorrelated, this means that the one-phonon imaginary-time Green's function, $G_{\mathbf{\Gamma}}^{\nu;\nu'}(t)$, is zero unless $\nu = \nu'$. It is also straightforward to show that $G_{\mathbf{q};\mathbf{\Gamma}}^{\nu\mu;\nu'}(t)$ and $G_{\mathbf{\Gamma};\mathbf{q}}^{\nu;\nu'\mu'}(t)$ is zero for all combinations. Lastly, for the second order, $G_{\mathbf{q};\mathbf{k}}^{\nu\mu;\nu'\mu'}(t)$, only modes that fulfill $\nu = \nu'$ and $\mu = \mu'$ will be non-zero, these modes are called combination modes. There is a special case of the above combination where, $\nu = \nu' = \mu = \mu'$, these modes are called overtones instead.

For an anharmonic system, these rules no longer apply, and no specific combination is necessarily zero. However, it is reasonable to assume that the largest contributions are indeed stemming from harmonically allowed Green's functions. Naturally, the phonon modes should have the strongest correlation with itself. Attempts have therefore been carried out to quantify the Raman spectrum in terms of overtones and combination modes [70].

6

Statistics and machine learning

One key aspect of machine learning is to know the biases and imperfections of your input data. This is, because, the model can only be as good as the data that it is given. It is, therefore, just as crucial to evaluate the input data as it is the final model. Moreover, solving the regression problem, Eq. (4.6), is a research field on its own, but a few straight forward solutions can easily be obtained. Therefore, in this chapter, a few key insights into how to solve Eq. (4.6), analyze the input data and evaluate the final model will be presented.

6.1 Regression

Regression methods estimate the relation between dependent variables, which is exactly what we are trying to do in Eq. (4.6). Below follows a few different linear regression methods.

6.1.1 Ordinary least squares

The simplest solution to Eq. (4.6) is the ordinary least squares solution which minimizes the root mean squared error (RMSE),

$$\min_{\mathbf{\Phi}} ||\mathbf{A\Phi} - \mathbf{F}||_2^2. \tag{6.1}$$

Since the function is convex, it is straight forward to find the global minimum,

$$\mathbf{\Phi} = (\mathbf{A}^T\mathbf{A})^{-1}\mathbf{A}^T\mathbf{F}. \tag{6.2}$$

This solution is, however, prone to overfitting. Meaning that, if we included features in the model that are irrelevant or unimportant, they will mostly contribute to fitting

noise in the input data, reducing the ability of the model to predict unseen data. The knowledge of which features are important in, e.g., the force constant expansion in Eq. (4.3) is not always self-evident and can sometimes be hard to judge prior to constructing the model, especially for higher order models. Therefore, it can be critical to use more advanced methods that remove or regularize unimportant features.

6.1.2 Regularization

Regularization is a class of algorithms that aims to minimize the RMSE together with a scaled penalty term, which is usually a norm of the feature vector. In Ridge ($n = 2$) and LASSO ($n = 1$), the object function is

$$\min_{\mathbf{\Phi}} \left\{ ||\mathbf{A}\mathbf{\Phi} - \mathbf{F}||_2^2 + \lambda ||\mathbf{\Phi}||_n \right\}$$

where $||\mathbf{\Phi}||_n$ is the ℓ_n norm of $\mathbf{\Phi}$ and λ is a hyperparameter. A larger λ in LASSO leads to a sparser model (fewer features) and a smaller λ leads to a denser model (more features). Denser models tend to describe seen data very well, however, depending on the problem they can sometimes describe unseen data rather poorly. On the other hand, a larger λ in ridge does not necessarily lead to a sparse model, but rather, that the features tend to have a smaller magnitude. Ridge typically leads to a smoother function, which is desirable, since this avoids fitting of noise. However, Fransson *et al.* [161], found that other machine learning methods might be more suited for FCs fitting, such as ARDR or RFE.

Linear support vector regression is another type of regularization method, which, similarly to LASSO and Ridge penalizes large parameters. The difference lies in the objective function. The RMSE part of the object function has been replaced with a part that allows for small errors in the training data,

$$\min_{\mathbf{\Phi}} \left\{ \frac{1}{2} ||\mathbf{\Phi}||_2^2 + C \sum_i^l (\xi_i + \xi_i^*) \right\}.$$

C is a user defined constant which controls the trade-off between the smoothness of the function and how well the training data is described. ξ_i and ξ_i^* are slack parameters, which penalizes predictions that lie above or below a "tube" of acceptable errors defined by the error margin, ϵ. The problem can also be formulated in a slightly more explicit form,

$$\min_{\mathbf{\Phi}} \left\{ \frac{1}{2} ||\mathbf{\Phi}||_2^2 + C \sum_i^l \max \left(0, |y_i - A_{ji}\Phi_i| - \epsilon \right) \right\}.$$

Thus, the idea is similar to ridge, we want the features to be as small as possible, or rather, the function to be as smooth as possible. This is done by having some acceptable
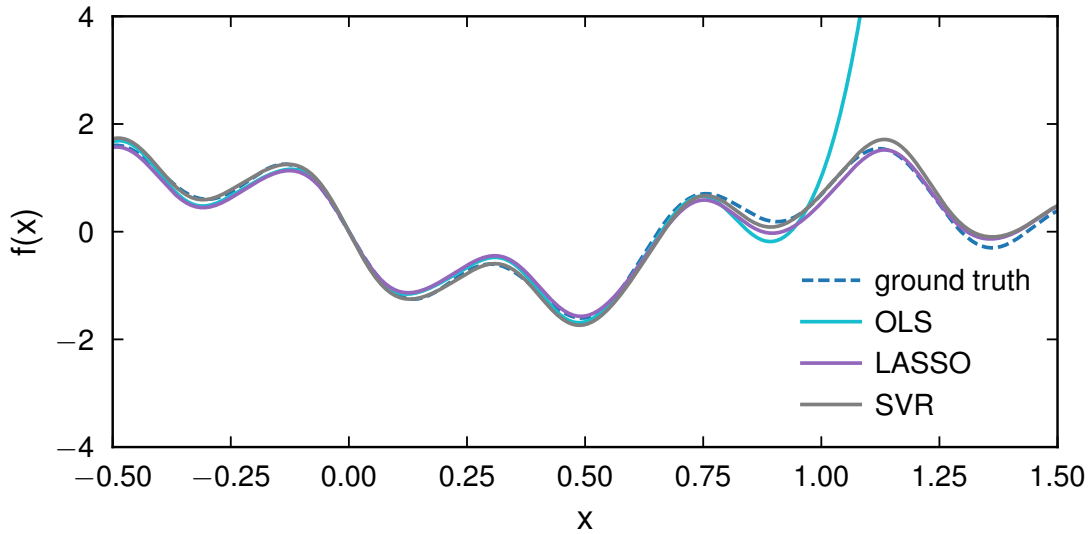
Figure 6.1: Comparing ordinary least squares (OLS), LASSO and Linear support vector regression (SVR) for a fictive regression problem

errors in the prediction, but too large errors gets penalized, for further information, see Ref. [162].

To demonstrate the strength of regularization, an arbitrary function is constructed as superposition of 4 sinusoidal waves. The amplitude acts as the parameter that we want to find and the wave act as the basis. To add some complexity, 3 more sinusoidal waves were included as basis functions. The function were sampled with 90 points that were randomly generated between 0 and 1 and a Gaussian noise, $\mathcal{N}(0, 0.6)$, was added. The resulting function and features are presented in Fig. 6.1 and Table 6.1, respectively. Ordinary least squares represents the function very well inside the region where the samples have been drawn, however, it severely overestimates the function for x values larger than 1. We note that this is due to the severely over/underestimated coefficients. The regularized methods on the other hand describe the function significantly better, even outside the sampled region, with more reasonable features. Fortunately, this artificial problem is not a good representation of the FCs problem, where ordinary least

ground truth	0.856	0	0.99	0.47	0.62	0	0
OLS	1329.44	2483.43	-50.07	1384.53	0.66	0.06	-1445.98
LASSO	0.00	0.00	0.62	0.00	0.63	0.04	-0.52
SVR	0.08	-0.22	0.79	-0.06	0.65	0.04	-0.39

Table 6.1: Amplitude of sinus wave with random frequency.

squares actually performs decently, but it highlights the properties of the penalty term in the extreme cases.

6.1.3 Bayesian methods

Another set of regression methods is the Bayesian methods which utilizes Bayes theorem,

$$p(\mathbf{\Phi}|\mathbf{F}) = \frac{p(F|\mathbf{\Phi})p(\mathbf{\Phi})}{p(\mathbf{F})}, \tag{6.3}$$

where $p(\mathbf{\Phi}|F)$ is the posterior, $p(F|\mathbf{\Phi})$ the likelihood, $p(\mathbf{\Phi})$ are the prior and $p(\mathbf{F})$ the marginal likelihood. A typical algorithm from this formalism is, e.g., ARDR [163], where the prior over the features is constructed as a centered elliptical Gaussian. By imposing hyperpriors it is possible to find the variance of the parameters and the standard deviation of the likelihood. ARDR allows for pruning of features with a slim distribution, i.e., features that most likely are irrelevant. The feature values that maximize the posterior is then taken as the solution. Conveniently, this formalism also allows us to draw parameters from the posterior to investigate the uncertainty of properties that are of interest, e.g., the phonon dispersion (see Chapter 4). The posterior can also be used to marginalize out the parameters and sample the uncertainty of new points.

An interesting note here is that some regularization algorithms can be understood from this formalism. For example, the ridge solution is the maximum posterior estimate of a Gaussian likelihood and a centered spherical Gaussian prior.

6.2 Correlation and condition number

The likelihood in Equation (6.3) is commonly assumed to be a normal distribution (as in the case of ARDR),

$$\begin{aligned} p(\mathbf{F}|, \mathbf{\Phi}, \sigma) &= \frac{1}{(2\pi\sigma)^{N_h}}\exp\left(-\frac{1}{2\sigma^2}(\mathbf{A\Phi} - \mathbf{F})^T(\mathbf{A\Phi} - \mathbf{F})\right) \\ &\propto \exp\left(-\frac{1}{2\sigma^2}(\mathbf{\Phi} - \tilde{\mathbf{\Phi}})^T(\mathbf{A}^T\mathbf{A})(\mathbf{\Phi} - \tilde{\mathbf{\Phi}})\right). \end{aligned} \tag{6.4}$$

Then, if we assume a uniform prior for the parameters, $\mathbf{\Phi} \sim \mathcal{U}$, the posterior, which is a distribution of the features, $\mathbf{\Phi}$, will be directly proportional to the likelihood. In that case, we can identify the mean and covariance matrix of the features as,

$$\begin{aligned} \mathbf{\Sigma} &= (\sigma^{-2}\mathbf{A}^T\mathbf{A})^{-1} \\ \tilde{\mathbf{\Phi}} &= \frac{1}{\sigma^2}\mathbf{\Sigma}\mathbf{A}^T\mathbf{F}. \end{aligned} \tag{6.5}$$

Where $\tilde{\boldsymbol{\Phi}}$ is the ordinary least squares solution given in Eq. (6.2) and $C = \mathbf{A}^T\mathbf{A}$ is the cross-correlation matrix. For the best possible solution, we want the inversion of the cross-correlation matrix to be as well posed as possible. This means that, the cross-correlation matrix should include as much information as possible for each feature. That is, the data should ideally be drawn as if it were independent data. The cross-correlation matrix for such data will have a very slim distribution for the off-diagonal elements, see, e.g., Ref. [164] for more details.

Another related method of estimating how well posed the regression problem in Eq. (4.6) is, is the condition number. The condition number is the ratio of the largest and smallest singular value of the design matrix. These singular values are calculated as the square root of the eigenvalues of the cross-correlation matrix. Hence, the condition number tells you the worst scaling ratio of two general vectors multiplied by the design matrix. For an ill-conditioned problem, the condition number would be large, i.e, the scaling between two general vectors is very different. A severely conditioned problem have two or more linearly dependent columns in the design matrix, which gives an infinite condition number.

To demonstrate an example of correlations and the condition number, three design matrices were constructed for BZO. Only harmonic interactions were considered, the cutoff was set to 8 Å and the total number of features were 102. The snapshots were generated from the rattle, phonon, and MD methods. The standard deviation of the rattled structures were set to 0.05 Å, and the temperature for the phonon and MD structures were 300 K. The columns in the design matrix, A, has been standardized, i.e., the distribution of the training data for a single feature has a standard deviation of one. Fig. 6.2 then shows the correlations between three harmonic features, ideally, the distributions should be the shape of a circle. However, as the figure depicts, the features have more or less the shape of an ellipse, meaning that the features are, to some extent, correlated. Moreover, the condition number and the average, minimum and maximum value from the cross-correlation matrix are summarized in Table 6.2, which has been multiplied by 10^3 and normalized as described in [164]. For this specific example, the correlations between the features in the rattle snapshots seems to be on average the lowest. However, no general trends or conclusions between the three ways of generating snapshots can

	C_{min}	C_{max}	C_{mean}	condition number
rattle	0.0000	1.2545	0.0278	41.3469
phonon	0.0000	5.8271	0.0885	57.4894
MD	0.0000	1.3010	0.0361	69.0985

Table 6.2: Condition number, minimum, maximum, and average correlation for the harmonic features of BZO within a cutoff of 8 Å. The total number of features are 102.
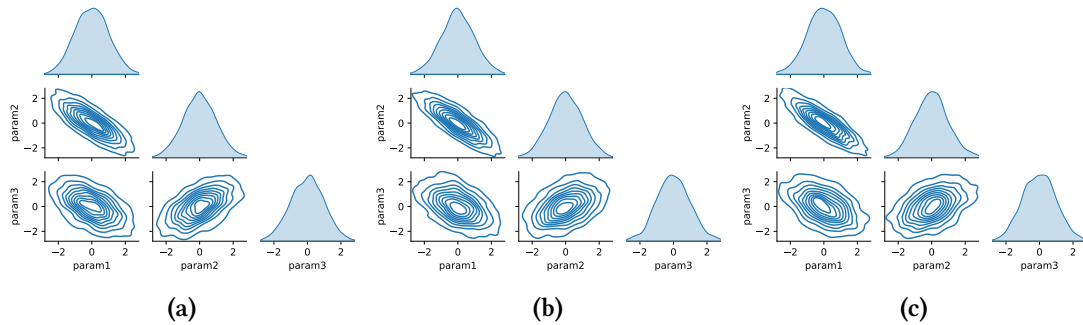
Figure 6.2: Visualization of correlations of the three most short ranged parameters in a training set from (a) rattle, (b) phonon and, (c) MD

be drawn from this minimal analysis, that is, this serves only as an example.

6.2.1 Model performance

Finally, the performance of the model can be evaluated through cross validation, which measures how well the model is at predicting unseen data. Cross validation splits your data set into several different training and validation sets. The model is trained on the training set and tested on the validation set. This is repeated for all of the splits, and in the end you can check the performance of the model by, e.g., calculating an average score. The score is calculated via a loss function, a common loss function is the RMSE. The splits can be done in several different ways, but two has mainly been explored in this thesis, namely shuffle-split and KFold. KFold divides the data into k sets, each set is then chosen once as a validation set, and the others are used as training examples. Shuffle-split randomizes x number of validation examples in each iteration and the rest serves as training examples. The benefit of shuffle-split is that you can do as many splits as you'd like without making the training set smaller, which is a restriction of KFold. The benefit of KFold is that all data are used at least once as a validation set, which is not guaranteed in shuffle-split.

However, there are other functions that in addition to minimizing the error penalize the number of non-zero features in the model. One such function is the Bayesian information criterion,

$$\text{BIC} = k \ln n - 2 \ln \hat{L}, \tag{6.6}$$

where k is the number of non-zero features, n is the number of samples and $\hat{L}$ is the maximized value of the likelihood function. The model with the smallest Bayesian information criterion value is the best model. The idea behind the Bayesian information criterion is that it is an approximation of the marginal likelihood (or model evidence), i.e., it is related to the probability that you will observe the training data with a specific

model,

$$p(\mathbf{F}|M) \approx \exp\left(-\frac{\text{BIC}}{2}\right)$$

where M is the model. It is noteworthy that the Bayesian information criterion is calculated on the whole training set, i.e., there are no cross validation splits when evaluating a model using the Bayesian information criterion. Commonly, both Bayesian information criterion and cross-validation are used in tandem to evaluate the performance of the model.

7

Summary of my work

When I started my PhD in the beginning of 2020 our research group had just finished a project on the ground-state structure of barium zirconate [65]. This was a joint collaboration between theory and experiments, and the conclusion of the project was that barium zirconate remained cubic down to essentially zero kelvin. However, the theoretical simulations were limited to the quasi-harmonic approximation and the results were very sensitive to the employed exchange-correlation functional. Moreover, the experimental work was done on a powder sample, limiting the ability to conclusively extract the frequency of the oxygen octahedra tilt mode. Producing a high quality single crystal of barium zirconate has been an ongoing challenge for the experimentalist due to the high temperatures needed for the manufacturing.

At that time, we got in contact with a research group in France that had successfully grown a single crystal of barium zirconate. They had subsequently contacted a group in Luxembourg that had conducted neutron scattering experiments of high quality for low temperatures and extracted the temperature dependence of a couple of phonon modes. This initiated the collaboration of **PAPER I**.

We used a software package, HIPHIVE, that could extract higher order force constants from randomly displaced structures. This software package had been developed by our group and was finalized a short time after the project on the ground-state structure of barium zirconate in Ref [65]. This meant that we could now utilize this to software to construct a model of the force constants for barium zirconate in order to go beyond the quasi-harmonic approximation. This model was then used to perform self-consistent phonons and molecular dynamics to calculate the frequency dependence of the tilt mode, including quantum effects and anharmonicity. The collaboration was successful, and we cemented that barium zirconate is cubic down to essentially zero kelvin. One of the results from that project was a calculation of the phonon dispersion, including quantum effects. This calculation was carried out at various temperatures
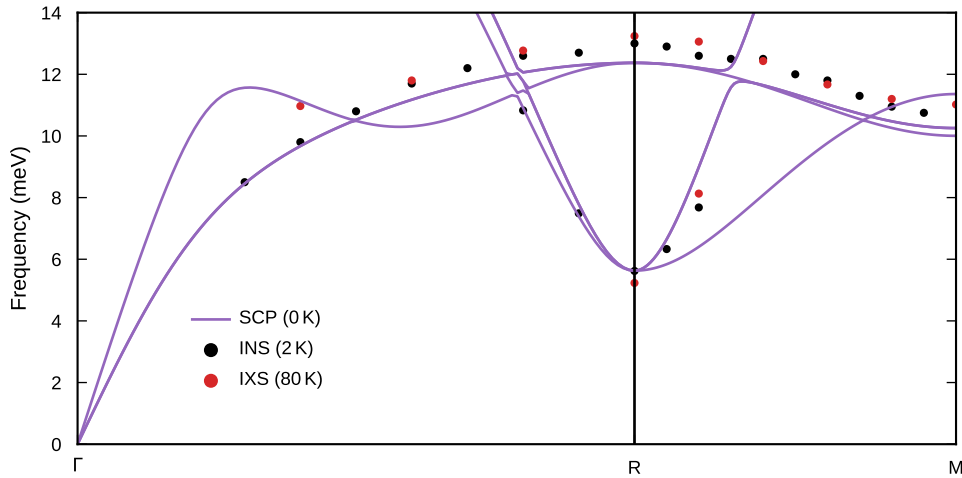
Figure 7.1: Phonon dispersion calculated with self-consistent phonons at 0 K calculated with a force constant potential based on PBE. This is plotted together with experimental data from inelastic neutron scattering and inelastic X-ray scattering at 2 K and 80 K, respectively.

with self-consistent phonons. In Fig. 7.1 the calculations at 0 K is shown together with experimental data at 2 K and 80 K.

Still, some questions remained about the structure of barium zirconate, more specifically of the local structure. Indeed, experimentally, it has been confirmed that barium zirconate has a long range order that is of cubic nature. However, this does not necessarily mean that the short range order have to be cubic. In particular, Raman experiments have indicated that barium zirconate may exhibit deviations from the cubic structure at the local scale. These deviations are believed to result from local regions of correlated octahedral tilts, known as nanodomains. A study from 2000 by Chemarin *et al.* [74] found that the Raman spectrum of barium zirconate exhibited sharp features which were reminiscent of first order scattering. A more recent article echoed the same sentiment [63]. They compared the Raman spectrum of barium zirconate to a very similar material, strontium titanate which is also cubic. However, the stark difference between the two indicated to the authors that the peaks in barium zirconate had to be first order scattering. In a recent study [64], an experimental group in the USA had conducted electron diffraction experiments on barium zirconate. They found a speckle at the R-point below 80 K and claimed that this speckle might be related to a local symmetry reduction. This caught our attention, and we thought that it would be interesting to study the electron diffraction experiments theoretically.

At this time, our research group was involved in developing machine learning potentials, specifically, the neuroevolution potential [130] and together with Erik Fransson we developed such a model for barium zirconate. Thanks to how efficient this model
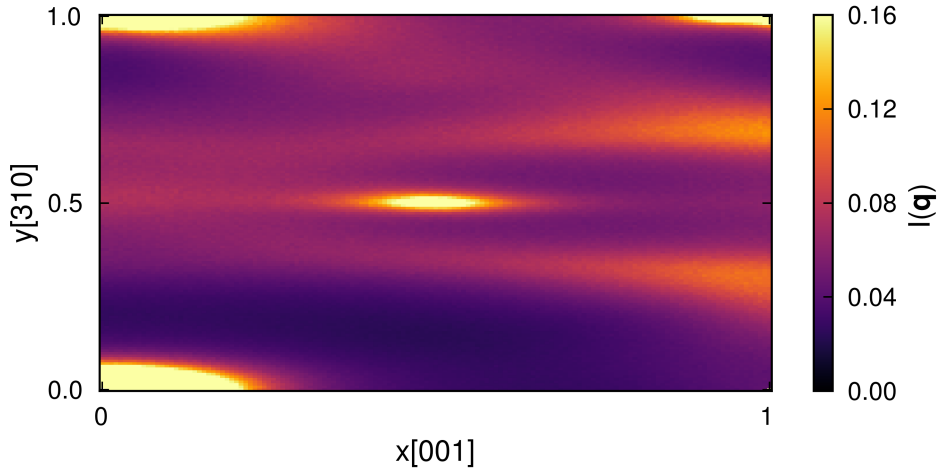
Figure 7.2: Simulated electron diffraction at 40 K in a 144 × 144 × 144 cubic supercell. The center of the plot correspondence to the R-point.

is, we could run really large scale simulations, roughly 15 million atoms for 100 ps, and achieve a very high resolution of the electron diffraction experiments. This was carried out in **PAPER II**. The simulated electron diffraction experiment is depicted in Fig. 7.2 at 40 K. The center of the plot corresponds to the R-point and shows that we also observe a speckle at the R-point, despite the structure not showing any signs of a local symmetry reduction in our simulations. Thus, we concluded that the observed speckle in the electron diffraction experiment is due to the very slow dynamics of tilt mode close to the phase transition. This phenomenon is referred to as thermal diffuse scattering, which is common close to displacive phase transitions.

In addition to barium zirconate we studied cesium lead bromide in **PAPER III**, which is a halide perovskite. This perovskite is very anharmonic, especially in comparison with barium zirconate. The material is cubic above ~ 400 K and undergoes two phase transitions as the temperature is lowered, from cubic to tetragonal and then from tetragonal to an orthorhombic phase. These transitions are driven by the soft dynamics of the bromide octahedra.

Despite the many differences between barium zirconate and cesium lead bromide, there are similarities between them as well. For example, barium zirconate also undergoes a phase transition from cubic to tetragonal, however, this phase transition is instead induced by applying a pressure. Moreover, both materials, close to the phase transition, exhibit very slow dynamics. This leads to long correlation times, and as mentioned above, results in thermal diffuse scattering but also large quasi-elastic scattering intensity. However, for cesium lead bromide, this slow dynamics also exist far away from the phase transition. This is different from barium zirconate where the slow
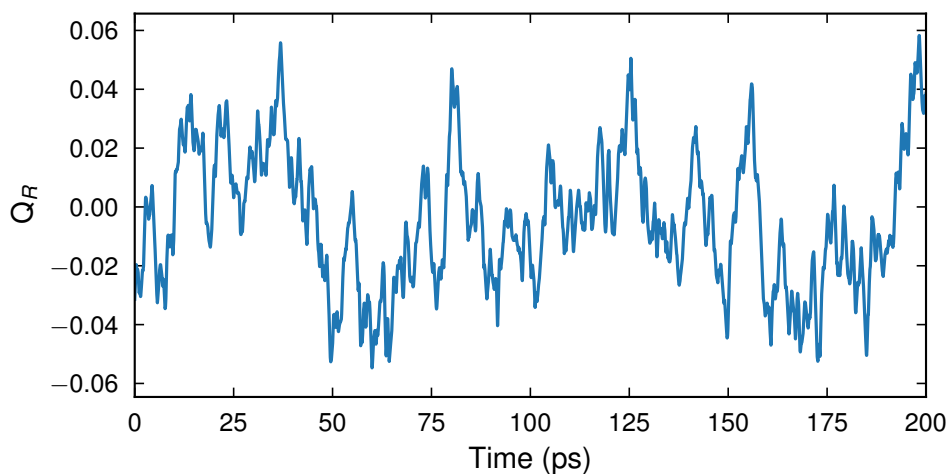
Figure 7.3: Phonon coordinate of the tilt mode close to the cubic to tetragonal phase transition of BZO, 16 GPa and 300 K, .

dynamics only appears very close to the phase transition.

In this paper, we also discussed the validity of the phonon quasiparticle picture. However, for slow dynamics, the lifetime is shorter than the period of the oscillation. This calls into question the validity of the phonon quasiparticle picture, as the dynamics is more akin to Brownian motion than oscillatory behavior in this regime. Fig. 7.3 illustrates the intriguing slow dynamics.

In **PAPER IV**, we extended the neuroevolution potential framework to predict rank one and two tensors, the model is referred to as tensorial neuroevolution potential. This means that we developed a machine learning model that can, e.g., quickly and accurately predict the total dipole moment and dielectric susceptibility for crystals and molecules. We compared the efficacy as well as efficiency compared to other similar models and found that the tensorial neuroevolution potential is an attractive option. This model could then be used in tandem with a regular potential to investigate the dynamics of molecules and solids. We also briefly discussed how light scattering works and how one can do it computationally using the neuroevolution potential together with a tensorial neuroevolution potential. Finally, we simulated the Raman and IR spectrum of barium zirconate, $PTAF^{-1}$ and liquid water.

We utilized the same model in **PAPER V** to investigate the Raman spectrum of barium zirconate as a function of pressure. This allowed us to further elucidate on the local structure by unraveling the origin of the sharp Raman features. We found that these features are stemming from exceptionally sharp second order Raman scattering, which further cements that barium zirconate both has a long- and short range cubic order. Moreover, we also note that, despite the cubic phase of barium zirconate which should
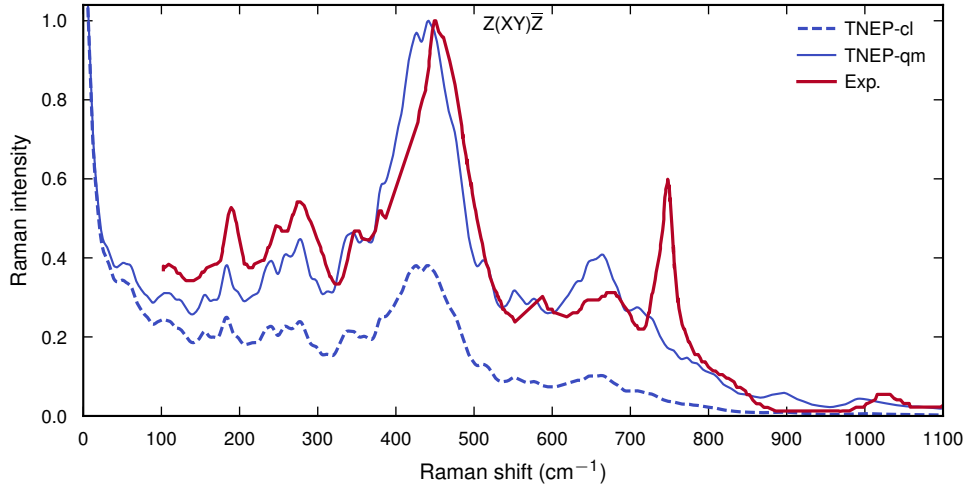
Figure 7.4: Cross polarized, Z(XY)$\overline{\text{Z}}$, Raman spectrum of cubic BZO at 0 GPa and 300 K. The cl model is without corrections and the qm model includes quantum corrections and is compared with experiments.

lack any first order scattering, close to the phase transition a central peak appears. We speculate that this peak is due to higher order Raman scattering, but intimately related to the slow dynamics of the oxygen octahedra tilt mode. Fig. 7.4 shows our simulated cross-polarized spectrum Z(XY)$\overline{\text{Z}}$ together with the experimentally measured spectrum. In this figure, we use a simple way to correct for the quantum statistics, which is explained in **PAPER V**. The agreement between theory and experiments is undeniable.

Acknowledgments

Bibliography

[1]   J. D. Hunter, *Matplotlib: A 2D graphics environment,* Computing in Science & Engineering **9**, 90 (2007). `doi:10.1109/MCSE.2007.55`.

[2]   A. Stukowski, *Visualization and analysis of atomistic simulation data with OVITO-the Open Visualization Tool,* Modelling and Simulation in Materials Science and Engineering **18**, (2010). `doi:10.1088/0965-0393/18/1/015012`.

[3]   Inkscape Project, *Inkscape,* 2022. `https://inkscape.org`.

[4]   C. Duan, R. J. Kee, H. Zhu, C. Karakaya, Y. Chen, S. Ricote, A. Jarry, E. J. Crumlin, D. Hook, R. Braun, N. P. Sullivan, and R. O'Hayre, *Highly Durable, Coking and Sulfur Tolerant, Fuel-Flexible Protonic Ceramic Fuel Cells,* Nature **557**, 217 (2018). `doi:10.1038/s41586-018-0082-6`.

[5]   C. Duan, R. Kee, H. Zhu, N. Sullivan, L. Zhu, L. Bian, D. Jennings, and R. O'Hayre, *Highly Efficient Reversible Protonic Ceramic Electrochemical Cells for Power Generation and Fuel Production,* Nature Energy **4**, 230 (2019). `doi:10.1038/s41560-019-0333-2`.

[6]   E. Fabbri, L. Bi, D. Pergolesi, and E. Traversa, *Towards the Next Generation of Solid Oxide Fuel Cells Operating Below 600 ℃ with Chemically Stable Proton-Conducting Electrolytes,* Advanced Materials **24**, 195 (2012). `doi:10.1002/adma.201103102`.

[7]   E. D. Wachsman and K. T. Lee, *Lowering the Temperature of Solid Oxide Fuel Cells,* Science **334**, 935 (2011). `doi:10.1126/science.1204090`.

[8]   G. W. Crabtree, M. S. Dresselhaus, and M. V. Buchanan, *The Hydrogen Economy,* Physics Today **57**, 39 (2004). `doi:10.1063/1.1878333`.

[9]   J. Wang, Z. Li, H. Zang, Y. Sun, Y. Zhao, Z. Wang, Z. Zhu, Z. Wei, and Q. Zheng, *$BaZr_{0.1}Fe_{0.9-x}NixO_{3-\delta}$ Cubic Perovskite Oxides for Protonic Ceramic Fuel Cell Cathodes,* International Journal of Hydrogen Energy **47**, 9395 (2022). `doi:10.1016/j.ijhydene.2022.01.012`.

[10]   S. Wang, J. Shen, Z. Zhu, Z. Wang, Y. Cao, X. Guan, Y. Wang, Z. Wei, and M. Chen, *Further Optimization of Barium Cerate Properties via Co-Doping Strategy for Potential Application as Proton-Conducting Solid Oxide Fuel Cell Electrolyte,* Journal of Power Sources **387**, 24 (2018). `doi:10.1016/j.jpowsour.2018.03.054`.

[11]   M. A. Gomez, M. A. Griffin, S. Jindal, K. D. Rule, and V. R. Cooper, *The effect of octahedral tilting on proton binding sites and transition states in pseudo-cubic perovskite oxides,* The Journal of Chemical Physics **123**, 094703 (2005). `doi:10.1063/1.2035099`.

[12] A. Torayev, L. Sperrin, M. A. Gomez, J. A. Kattirtzi, C. Merlet, and C. P. Grey, *Local Distortions and Dynamics in Hydrated Y-Doped BaZrO₃,* The Journal of Physical Chemistry C **124**, 16689–16701 (2020). `doi:10.1021/acs.jpcc.0c04594`.

[13] N. Suresh Kumar and K. Chandra Babu Naidu, *A review on perovskite solar cells (PSCs), materials and applications,* Journal of Materiomics **7**, 940–956 (2021). `doi:10.1016/j.jmat.2021.04.002`.

[14] W. Zhu, Q. Zhang, C. Zhang, Z. Zhang, D. Chen, Z. Lin, J. Chang, J. Zhang, and Y. Hao, *Aged Precursor Solution toward Low-Temperature Fabrication of Efficient Carbon-Based All-Inorganic Planar CsPbIBr₂ Perovskite Solar Cells,* ACS Applied Energy Materials **1**, 4991–4997 (2018). `doi:10.1021/acsaem.8b00972`.

[15] G. Wang, J. Liu, M. Lei, W. Zhang, and G. Zhu, *Optimizing the substrate pre-heating and post-annealing temperatures for fabricating high-performance carbon-based CsPbIBr₂ inorganic perovskite solar cells,* Electrochimica Acta **349**, 136354 (2020). `doi:10.1016/j.electacta.2020.136354`.

[16] Y. Pei, H. Guo, Z. Hu, J. Zhang, and Y. Zhu, *BiBr₃ as an additive in CsPbBr₃ for carbon-based all-inorganic perovskite solar cell,* Journal of Alloys and Compounds **835**, 155283 (2020). `doi:10.1016/j.jallcom.2020.155283`.

[17] M. R. Filip, G. E. Eperon, H. J. Snaith, and F. Giustino, *Steric engineering of metal-halide perovskites with tunable optical band gaps,* Nature Communications **5**, 5757 (2014). `doi:10.1038/ncomms6757`.

[18] J. Wiktor, U. Rothlisberger, and A. Pasquarello, *Predictive Determination of Band Gaps of Inorganic Halide Perovskites,* The Journal of Physical Chemistry Letters **8**, 5507–5512 (2017). `doi:10.1021/acs.jpclett.7b02648`.

[19] G. Rose, *Mineralogisch-geognostische reise nach dem Ural, dem Altai un dem kaspischen meere* (Berlin, Verlag der Sanderschen buchandlung (C.W. Eichhoff), 1837).

[20] S. Jiang, T. Hu, J. Gild, N. Zhou, J. Nie, M. Qin, T. Harrington, K. Vecchio, and J. Luo, *A New Class of High-Entropy Perovskite Oxides,* Scripta Materialia **142**, 116 (2018). `doi:10.1016/j.scriptamat.2017.08.040`.

[21] C. M. Rost, E. Sachet, T. Borman, A. Moballegh, E. C. Dickey, D. Hou, J. L. Jones, S. Curtarolo, and J.-P. Maria, *Entropy-Stabilized Oxides,* Nature Communications **6**, 8485 (2015). `doi:10.1038/ncomms9485`.

[22] Y. Zhang, C.-K. Lim, Z. Dai, G. Yu, J. W. Haus, H. Zhang, and P. N. Prasad, *Photonics and Optoelectronics Using Nano-Structured Hybrid Perovskite Media and Their Optical Cavities,* Physics Reports **795**, 1 (2019). `doi:10.1016/j.physrep.2019.01.005`.

[23] A. Dey, J. Ye, A. De, E. Debroye, S. K. Ha, E. Bladt, A. S. Kshirsagar, Z. Wang, J. Yin, Y. Wang, L. N. Quan, F. Yan, M. Gao, X. Li, J. Shamsi, T. Debnath, M. Cao, M. A. Scheel, S. Kumar, J. A. Steele, M. Gerhard, L. Chouhan, K. Xu, X.-g. Wu, Y. Li, Y. Zhang, A. Dutta, C. Han, I. Vincon, A. L. Rogach, A. Nag, A. Samanta, B. A. Korgel, C.-J. Shih, D. R. Gamelin, D. H. Son, H. Zeng, H. Zhong, H. Sun, H. V. Demir, I. G. Scheblykin, I. Mora-Seró, J. K. Stolarczyk, J. Z. Zhang, J. Feldmann, J. Hofkens, J. M. Luther, J. Pérez-Prieto, L. Li, L. Manna, M. I. Bodnarchuk, M. V. Kovalenko, M. B. J. Roeffaers, N. Pradhan, O. F. Mohammed, O. M. Bakr, P. Yang, P. Müller-Buschbaum, P. V. Kamat, Q. Bao, Q. Zhang, R. Krahne,

R. E. Galian, S. D. Stranks, S. Bals, V. Biju, W. A. Tisdale, Y. Yan, R. L. Z. Hoye, and L. Polavarapu, *State of the Art and Prospects for Halide Perovskite Nanocrystals,* ACS Nano **15**, 10775 (2021). `doi:10.1021/acsnano.0c08903`.

[24] W.-J. Yin, J.-H. Yang, J. Kang, Y. Yan, and S.-H. Wei, *Halide Perovskite Materials for Solar Cells: A Theoretical Review,* Journal of Materials Chemistry A **3**, 8926 (2015). `doi:10.1039/C4TA05033A`.

[25] A. K. Jena, A. Kulkarni, and T. Miyasaka, *Halide Perovskite Photovoltaics: Background, Status, and Future Prospects,* Chemical Reviews **119**, 3036 (2019). `doi:10.1021/acs.chemrev.8b00539`.

[26] N. Wang, H. Toriumi, Y. Sato, C. Tang, T. Nakamura, K. Amezawa, S. Kitano, H. Habazaki, and Y. Aoki, $La_{0.8}Sr_{0.2}Co_{1-x}Ni_xO_{3-\delta}$ *as the Efficient Triple Conductor Air Electrode for Protonic Ceramic Cells,* ACS Applied Energy Materials **4**, 554 (2021). `doi:10.1021/acsaem.0c02447`.

[27] Y. Yamazaki, F. Blanc, Y. Okuyama, L. Buannic, J. C. Lucio-Vega, C. P. Grey, and S. M. Haile, *Proton Trapping in Yttrium-Doped Barium Zirconate,* Nature Materials **12**, 647 (2013). `doi:10.1038/nmat3638`.

[28] M.-H. Zhang, K. Wang, Y.-J. Du, G. Dai, W. Sun, G. Li, D. Hu, H. C. Thong, C. Zhao, X.-Q. Xi, Z.-X. Yue, and J.-F. Li, *High and Temperature-Insensitive Piezoelectric Strain in Alkali Niobate Lead-free Perovskite,* Journal of the American Chemical Society **139**, 3889 (2017). `doi:10.1021/jacs.7b00520`.

[29] I. H. Lone, J. Aslam, N. R. E. Radwan, A. H. Bashal, A. F. A. Ajlouni, and A. Akhter, *Multiferroic ABO_3 Transition Metal Oxides: A Rare Interaction of Ferroelectricity and Magnetism,* Nanoscale Research Letters **14**, 142 (2019). `doi:10.1186/s11671-019-2961-7`.

[30] H. Tamura, T. Konoike, Y. Sakabe, and K. Wakino, *Improved High-Q Dielectric Resonator with Complex Perovskite Structure,* Journal of the American Ceramic Society **67**, c59 (1984). `doi:10.1111/j.1151-2916.1984.tb18828.x`.

[31] W. Zhong, C.-T. Au, and Y.-W. Du, *Review of Magnetocaloric Effect in Perovskite-Type Oxides,* Chinese Physics B **22**, 057501 (2013). `doi:10.1088/1674-1056/22/5/057501`.

[32] V. M. Goldschmidt, *Die Gesetze der Krystallochemie,* Naturwissenschaften **14**, 477 (1926). `doi:10.1007/BF01507527`.

[33] R. D. Shannon, *Revised Effective Ionic Radii and Systematic Studies of Interatomic Distances in Halides and Chalcogenides,* Acta Crystallographica Section A **32**, 751 (1976). `doi:10.1107/S0567739476001551`.

[34] K. M. Rabe, C. H. Ahn, and J.-M. Triscone, eds., *Physics of Ferroelectrics: A Modern Perspective* (Berlin ; New York: Springer, 2007). ISBN 978-3-540-34590-9.

[35] S. Sasaki, C. T. Prewitt, J. D. Bass, and W. A. Schulze, *Orthorhombic Perovskite $CaTiO_3$ and $CdTiO_3$: Structure and Space Group,* Acta Crystallographica Section C Crystal Structure Communications **43**, 1668 (1987). `doi:10.1107/S0108270187090620`.

[36] M. Swift, A. Janotti, and C. G. Van de Walle, *Small Polarons and Point Defects in Barium Cerate,* Physical Review B **92**, 214114 (2015). `doi:10.1103/PhysRevB.92.214114`.

[37] P. C. Hohenberg and A. P. Krekhov, *An introduction to the Ginzburg–Landau theory of phase transitions and nonequilibrium patterns,* Physics Reports **572**, 1–42 (2015). `doi:10.1016/j.physrep.2015.01.001`.

[38] T. Riste, E. J. Samuelsen, K. Otnes, and J. Feder, *Critical behaviour of SrTiO₃ near the 105°K phase transition,* Solid State Communications **9**, 1455–1458 (1971). `doi:10.1016/0038-1098(71)90155-4`.

[39] S. Hayward and E. Salje, *Cubic-Tetragonal Phase Transition in SrTiO₃ Revisited: Landau Theory and Transition Mechanism,* Phase Transitions **68**, 501 (1999). `doi:10.1080/01411599908224530`.

[40] H. Hong, R. Xu, A. Alatas, M. Holt, and T.-C. Chiang, *Central peak and narrow component in x-ray scattering measurements near the displacive phase transition in SrTiO₃,* Physical Review B **78**, 104121 (2008). `doi:10.1103/PhysRevB.78.104121`.

[41] R. Mizaras and A. Loidl, *Central peak in SrTiO₃ studied by dielectric spectroscopy,* Physical Review B **56**, 10726–10729 (1997). `doi:10.1103/PhysRevB.56.10726`.

[42] K. B. Lyons and P. A. Fleury, *Phonon interactions and the dynamic central peak in SrTiO₃ near the structural phase transition,* Solid State Communications **23**, 477–480 (1977). `doi:10.1016/0038-1098(77)91011-0`.

[43] M. Holt, M. Sutton, P. Zschack, H. Hong, and T.-C. Chiang, *Dynamic Fluctuations and Static Speckle in Critical X-Ray Scattering from SrTiO₃,* Physical Review Letters **98**, 065501 (2007). `doi:10.1103/PhysRevLett.98.065501`.

[44] R. A. Cowley, W. J. L. Buyers, and G. Dolling, *Relationship of normal modes of vibration of strontium titanate and its antiferroelectric phase transition at 110°K,* Solid State Communications **7**, 181–184 (1969). `doi:10.1016/0038-1098(69)90720-0`.

[45] P. A. Fleury, J. F. Scott, and J. M. Worlock, *Soft Phonon Modes and the 110°K Phase Transition in SrTiO₃,* Physical Review Letters **21**, 16–19 (1968). `doi:10.1103/PhysRevLett.21.16`.

[46] W. Zhong and D. Vanderbilt, *Competing Structural Instabilities in Cubic Perovskites,* Physical Review Letters **74**, 2587 (1995). `doi:10.1103/PhysRevLett.74.2587`.

[47] B. T. M. Willis, *Thermal diffuse scattering of X-rays and neutrons.* In U. Shmueli, ed., *International Tables for Crystallography Volume B: Reciprocal space* (Dordrecht: Springer Netherlands, 2001). `doi:10.1107/97809553602060000563`.

[48] K. A. Müller and H. Burkard, *SrTiO₃: An intrinsic quantum paraelectric below 4 K,* Physical Review B **19**, 3593–3602 (1979). `doi:10.1103/PhysRevB.19.3593`.

[49] R. Xu, J. Huang, E. S. Barnard, S. S. Hong, P. Singh, E. K. Wong, T. Jansen, V. Harbola, J. Xiao, B. Y. Wang, S. Crossley, D. Lu, S. Liu, and H. Y. Hwang, *Strain-induced room-temperature ferroelectricity in SrTiO₃ membranes,* Nature Communications **11**, 3141 (2020). `doi:10.1038/s41467-020-16912-3`.

[50] X. N. Zhu, W. Zhang, and X. M. Chen, *Enhanced dielectric and ferroelectric characteristics in Ca-modified BaTiO₃ ceramics,* AIP Advances **3**, 082125 (2013). `doi:10.1063/1.4819482`.

[51] W. Zhong, D. Vanderbilt, and K. M. Rabe, *Phase Transitions in BaTiO₃ from First Principles,* Physical Review Letters **73**, 1861–1864 (1994). `doi:10.1103/PhysRevLett.73.1861`.

[52] A. V. Turik and A. G. Khasabov, *On the origin of ferroelectricity in PbTiO₃*, Ferroelectrics **237**, 65–71 (2000). `doi:10.1080/00150190008216233`.

[53] Z.-G. Li, M. Zacharias, Y. Zhang, F. Wei, Y. Qin, Y.-Q. Yang, L.-C. An, F.-F. Gao, W. Li, J. Even, and X.-H. Bu, *Origin of Phase Transitions in Inorganic Lead Halide Perovskites: Interplay between Harmonic and Anharmonic Vibrations*, ACS Energy Letters , (2023). `doi:10.1021/acsenergylett.3c00881`.

[54] R. Ben Sadok, D. Hammoutène, and N. Plugaru, *New Phase Transitions Driven by Soft Phonon Modes for CsPbBr₃: Density Functional Theory Study*, physica status solidi (b) **258**, 2000289 (2021). `doi:10.1002/pssb.202000289`.

[55] S. Schryver and A. Lamichhane, *Temperature-driven structural phase transitions in CsPbBr₃*, Solid State Communications **371**, 115237 (2023). `doi:10.1016/j.ssc.2023.115237`.

[56] Š. Svirskas, S. Balčiūnas, M. Šimėnas, G. Usevičius, M. Kinka, M. Velička, D. Kubicki, M. E. Castillo, A. Karabanov, V. V. Shvartsman, M. d. R. Soares, V. Šablinskas, A. N. Salak, D. C. Lupascu, and J. Banys, *Phase transitions, screening and dielectric response of CsPbBr₃*, Journal of Materials Chemistry A **8**, 14015–14022 (2020). `doi:10.1039/D0TA04155F`.

[57] C. C. Stoumpos, C. D. Malliakas, J. A. Peters, Z. Liu, M. Sebastian, J. Im, T. C. Chasapis, A. C. Wibowo, D. Y. Chung, A. J. Freeman, B. W. Wessels, and M. G. Kanatzidis, *Crystal Growth of the Perovskite Semiconductor CsPbBr₃: A New Material for High-Energy Radiation Detection*, Crystal Growth & Design **13**, 2722–2727 (2013). `doi:10.1021/cg400645t`.

[58] S. Sharma, N. Weiden, and A. Weiss, *Phase Transitions in CsSnCl₃ and CsPbBr₃ An NMR and NQR Study*, Zeitschrift für Naturforschung A **46**, 329–336 (1991). `doi:10.1515/zna-1991-0406`.

[59] M. Rodová, J. Brožek, K. Knížek, and K. Nitsch, *Phase transitions in ternary caesium lead bromide*, Journal of Thermal Analysis and Calorimetry **71**, 667–673 (2003). `doi:10.1023/A:1022836800820`.

[60] D. Malyshkin, V. Sereda, I. Ivanov, M. Mazurin, A. Sednev-Lugovets, D. Tsvetkov, and A. Zuev, *New phase transition in CsPbBr₃*, Materials Letters **278**, 128458 (2020). `doi:10.1016/j.matlet.2020.128458`.

[61] S. Hirotsu, J. Harada, M. Iizumi, and K. Gesi, *Structural Phase Transitions in CsPbBr₃*, Journal of the Physical Society of Japan **37**, 1393–1398 (1974). `doi:10.1143/JPSJ.37.1393`.

[62] A. R. Akbarzadeh, I. Kornev, C. Malibert, L. Bellaiche, and J. M. Kiat, *Combined Theoretical and Experimental Study of the Low-Temperature Properties of BaZrO₃*, Physical Review B **72**, 205104 (2005). `doi:10.1103/PhysRevB.72.205104`.

[63] F. Giannici, M. Shirpour, A. Longo, A. Martorana, R. Merkle, and J. Maier, *Long-Range and Short-Range Structure of Proton-Conducting Y:BaZrO₃*, Chemistry of Materials **23**, 2994 (2011). `doi:10.1021/cm200682d`.

[64] I. Levin, M. G. Han, H. Y. Playford, V. Krayzman, Y. Zhu, and R. A. Maier, *Nanoscale-Correlated Octahedral Rotations in BaZrO₃*, Physical Review B **104**, 214109 (2021). `doi:10.1103/PhysRevB.104.214109`.

[65] A. Perrichon, E. Jedvik Granhed, G. Romanelli, A. Piovano, A. Lindman, P. Hyldgaard, G. Wahnström, and M. Karlsson, *Unraveling the Ground-State Structure of BaZrO$_3$ by Neutron Scattering Experiments and First-Principles Calculations,* Chemistry of Materials **32**, 2824 (2020). `doi:10.1021/acs.chemmater.9b04437`.

[66] R. A. Evarestov, *Hybrid Density Functional Theory LCAO Calculations on Phonons in Ba(Ti,Zr,Hf)O$_3$,* Physical Review B **83**, 014105 (2011). `doi:10.1103/PhysRevB.83.014105`.

[67] T. S. Bjørheim, E. A. Kotomin, and J. Maier, *Hydration Entropy of BaZrO$_3$ from First Principles Phonon Calculations,* Journal of Materials Chemistry A **3**, 7639 (2015). `doi:10.1039/C4TA06880G`.

[68] A. I. Lebedev and I. A. Sluchinskaya, *Structural Instability in BaZrO$_3$ Crystals: Calculations and Experiment,* Physics of the Solid State **55**, 1941 (2013). `doi:10.1134/S1063783413090229`.

[69] A. Bilić and J. D. Gale, *Ground State Structure of BaZrO$_3$: A Comparative First-Principles Study,* Physical Review B **79**, 174107 (2009). `doi:10.1103/PhysRevB.79.174107`.

[70] C. Toulouse, D. Amoroso, C. Xin, P. Veber, M. C. Hatnean, G. Balakrishnan, M. Maglione, P. Ghosez, J. Kreisel, and M. Guennou, *Lattice Dynamics and Raman Spectrum of BaZrO$_3$ Single Crystals,* Physical Review B **100**, 134102 (2019). `doi:10.1103/PhysRevB.100.134102`.

[71] B. Guillaume, F. Boschini, I. Garcia-Cano, A. Rulmont, R. Cloots, and M. Ausloos, *Optimization of BaZrO$_3$ Sintering by Control of the Initial Powder Size Distribution; a Factorial Design Statistical Analysis,* Journal of the European Ceramic Society **25**, 3593 (2005). `doi:10.1016/j.jeurceramsoc.2004.09.022`.

[72] I. Charrier-Cougoulic, T. Pagnier, and G. Lucazeau, *Raman Spectroscopy of Perovskite-Type BaCe$_x$Zr$_{1-x}$O$_3$(0≤x≤1),* Journal of Solid State Chemistry **142**, 220 (1999). `doi:10.1006/jssc.1998.8038`.

[73] X. Yang, Q. Li, R. Liu, B. Liu, H. Zhang, S. Jiang, J. Liu, B. Zou, T. Cui, and B. Liu, *Structural Phase Transition of BaZrO$_3$ under High Pressure,* Journal of Applied Physics **115**, 124907 (2014). `doi:10.1063/1.4868906`.

[74] C. Chemarin, N. Rosman, T. Pagnier, and G. Lucazeau, *A High-Pressure Raman Study of Mixed Perovskites BaCe$_x$Zr$_{1-x}$O$_3$ (0≤x≤1),* Journal of Solid State Chemistry **149**, 298–307 (2000). `doi:10.1006/jssc.1999.8530`.

[75] M. Born and R. Oppenheimer, *Zur Quantentheorie Der Molekeln,* Annalen der Physik **389**, 457 (1927). `doi:10.1002/andp.19273892002`.

[76] P. L. Taylor and O. Heinonen, *A Quantum Approach to Condensed Matter Physics* (Cambridge: Cambridge University Press, 2002). ISBN 978-0-521-77103-0. `doi:10.1017/CBO9780511998782`.

[77] P. Hohenberg and W. Kohn, *Inhomogeneous Electron Gas,* Physical Review **136**, B864 (1964). `doi:10.1103/PhysRev.136.B864`.

[78] L. H. Thomas, *The Calculation of Atomic Fields,* Mathematical Proceedings of the Cambridge Philosophical Society **23**, 542 (1927). `doi:10.1017/S0305004100011683`.

[79] E. Fermi, *Un Metodo Statistico per La Determinazione Di Alcune Priorieta Dell'atome,* Rend. Accad. Naz. Lincei **6**, 602 (1927).

[80] P. A. M. Dirac, *Note on Exchange Phenomena in the Thomas Atom,* Mathematical Proceedings of the Cambridge Philosophical Society **26**, 376 (1930). `doi:10.1017/S0305004100016108`.

[81] W. Kohn and L. J. Sham, *Self-Consistent Equations Including Exchange and Correlation Effects,* Physical Review **140**, A1133 (1965). `doi:10.1103/PhysRev.140.A1133`.

[82] A. D. Becke, *Perspective: Fifty Years of Density-Functional Theory in Chemical Physics,* The Journal of Chemical Physics **140**, 18A301 (2014). `doi:10.1063/1.4869598`.

[83] R. O. Jones, *Density Functional Theory: Its Origins, Rise to Prominence, and Future,* Reviews of Modern Physics **87**, 897 (2015). `doi:10.1103/RevModPhys.87.897`.

[84] W. Kohn, *Nobel Lecture: Electronic Structure of Matter—Wave Functions and Density Functionals,* Reviews of Modern Physics **71**, 1253 (1999). `doi:10.1103/RevModPhys.71.1253`.

[85] R. M. Martin, *Electronic Structure: Basic Theory and Practical Methods* (Cambridge University Press, 2020). ISBN 978-1-108-65747-1.

[86] E. Wigner, *Effects of the Electron Interaction on the Energy Levels of Electrons in Metals,* Transactions of the Faraday Society **34**, 678 (1938). `doi:10.1039/TF9383400678`.

[87] E. Wigner, *On the Interaction of Electrons in Metals,* Physical Review **46**, 1002 (1934). `doi:10.1103/PhysRev.46.1002`.

[88] M. Gell-Mann and K. A. Brueckner, *Correlation Energy of an Electron Gas at High Density,* Physical Review **106**, 364 (1957). `doi:10.1103/PhysRev.106.364`.

[89] D. M. Ceperley and B. J. Alder, *Ground State of the Electron Gas by a Stochastic Method,* Physical Review Letters **45**, 566 (1980). `doi:10.1103/PhysRevLett.45.566`.

[90] J. P. Perdew, K. Burke, and M. Ernzerhof, *Generalized Gradient Approximation Made Simple,* Physical Review Letters **77**, 3865 (1996). `doi:10.1103/PhysRevLett.77.3865`.

[91] M. G. Medvedev, I. S. Bushmarinov, J. Sun, J. P. Perdew, and K. A. Lyssenko, *Density Functional Theory Is Straying from the Path toward the Exact Functional,* Science **355**, 49 (2017). `doi:10.1126/science.aah5975`.

[92] J. P. Perdew and A. Zunger, *Self-Interaction Correction to Density-Functional Approximations for Many-Electron Systems,* Physical Review B **23**, 5048 (1981). `doi:10.1103/PhysRevB.23.5048`.

[93] J. P. Perdew and M. Levy, *Physical Content of the Exact Kohn-Sham Orbital Energies: Band Gaps and Derivative Discontinuities,* Physical Review Letters **51**, 1884 (1983). `doi:10.1103/PhysRevLett.51.1884`.

[94] P. Mori-Sánchez, A. J. Cohen, and W. Yang, *Localization and Delocalization Errors in Density Functional Theory and Implications for Band-Gap Prediction,* Physical Review Letters **100**, 146401 (2008). `doi:10.1103/PhysRevLett.100.146401`.

[95] S. L. Dudarev, G. A. Botton, S. Y. Savrasov, C. J. Humphreys, and A. P. Sutton, *Electron-Energy-Loss Spectra and the Structural Stability of Nickel Oxide: An LSDA+U Study,* Physical Review B **57**, 1505 (1998). `doi:10.1103/PhysRevB.57.1505`.

[96] H. J. Kulik, *Perspective: Treating Electron over-Delocalization with the DFT+U Method,* The Journal of Chemical Physics **142**, 240901 (2015). `doi:10.1063/1.4922693`.

[97] E. J. Granhed, A. Lindman, C. Eklöf-Österberg, M. Karlsson, S. F. Parker, and G. Wahnström, *Band vs. Polaron: Vibrational Motion and Chemical Expansion of Hydride Ions as Signatures for the Electronic Character in Oxyhydride Barium Titanate,* Journal of Materials Chemistry A **7**, 16211 (2019). `doi:10.1039/C9TA00086K`.

[98] J. P. Perdew, M. Ernzerhof, and K. Burke, *Rationale for Mixing Exact Exchange with Density Functional Approximations,* The Journal of Chemical Physics **105**, 9982 (1996). `doi:10.1063/1.472933`.

[99] J. Paier, R. Hirschl, M. Marsman, and G. Kresse, *The Perdew–Burke–Ernzerhof Exchange-Correlation Functional Applied to the G2-1 Test Set Using a Plane-Wave Basis Set,* The Journal of Chemical Physics **122**, 234102 (2005). `doi:10.1063/1.1926272`.

[100] A. V. Krukau, O. A. Vydrov, A. F. Izmaylov, and G. E. Scuseria, *Influence of the Exchange Screening Parameter on the Performance of Screened Hybrid Functionals,* The Journal of Chemical Physics **125**, 224106 (2006). `doi:10.1063/1.2404663`.

[101] W. E. Pickett, *Pseudopotential Methods in Condensed Matter Applications,* Computer Physics Reports **9**, 115 (1989). `doi:10.1016/0167-7977(89)90002-6`.

[102] D. R. Hamann, M. Schlüter, and C. Chiang, *Norm-Conserving Pseudopotentials,* Physical Review Letters **43**, 1494 (1979). `doi:10.1103/PhysRevLett.43.1494`.

[103] D. Vanderbilt, *Soft Self-Consistent Pseudopotentials in a Generalized Eigenvalue Formalism,* Physical Review B **41**, 7892 (1990). `doi:10.1103/PhysRevB.41.7892`.

[104] P. E. Blöchl, *Projector Augmented-Wave Method,* Physical Review B **50**, 17953 (1994). `doi:10.1103/PhysRevB.50.17953`.

[105] A. Togo and I. Tanaka, *First Principles Phonon Calculations in Materials Science,* Scripta Materialia **108**, 1 (2015). `doi:10.1016/j.scriptamat.2015.07.021`.

[106] F. Eriksson, E. Fransson, and P. Erhart, *The Hiphive Package for the Extraction of High-Order Force Constants by Machine Learning,* Advanced Theory and Simulations **2**, 1800184 (2019). `doi:10.1002/adts.201800184`.

[107] K. Parlinski, Z. Q. Li, and Y. Kawazoe, *First-Principles Determination of the Soft Mode in Cubic* ZrO_2, Physical Review Letters **78**, 4063 (1997). `doi:10.1103/PhysRevLett.78.4063`.

[108] X. Gonze, J.-C. Charlier, D. Allan, and M. Teter, *Interatomic Force Constants from First Principles: The Case of α-Quartz,* Physical Review B **50**, 13035 (1994). `doi:10.1103/PhysRevB.50.13035`.

[109] B. Fultz, *Vibrational Thermodynamics of Materials,* Progress in Materials Science **55**, 247 (2010). `doi:10.1016/j.pmatsci.2009.05.002`.

[110] J. J. Sakurai and J. Napolitano, *Modern Quantum Mechanics* (Cambridge University Press, 2020). ISBN 978-1-108-58728-0. `doi:10.1017/9781108587280`.

[111] S. Rossano, F. Mauri, C. J. Pickard, and I. Farnan, *First-Principles Calculation of* ^{17}O *and* ^{25}Mg *NMR Shieldings in MgO at Finite Temperature: Rovibrational Effect in Solids,* The Journal of Physical Chemistry B **109**, 7245 (2005). `doi:10.1021/jp044251w`.

[112] R. Mattuck, *A Guide to Feynman Diagrams in the Many-body Problem* (Dover Publications, 1992). ISBN 9780486670478. `https://books.google.se/books?id=pe-v8zfxE68C`.

[113] T. Tadano and S. Tsuneyuki, *Self-Consistent Phonon Calculations of Lattice Dynamical Properties in Cubic SrTiO₃ with First-Principles Anharmonic Force Constants,* Physical Review B **92**, 054301 (2015). `doi:10.1103/PhysRevB.92.054301`.

[114] L. Monacelli, R. Bianco, M. Cherubini, M. Calandra, I. Errea, and F. Mauri, *The stochastic self-consistent harmonic approximation: calculating vibrational properties of materials with full quantum and anharmonic effects,* Journal of Physics: Condensed Matter **33**, 363001 (2021). `doi:10.1088/1361-648X/ac066b`.

[115] N. Benshalom, G. Reuveni, R. Korobko, O. Yaffe, and O. Hellman, *Dielectric response of rock-salt crystals at finite temperatures from first principles,* Physical Review Materials **6**, 033607 (2022). `doi:10.1103/PhysRevMaterials.6.033607`.

[116] A. Togo, L. Chaput, and I. Tanaka, *Distributions of Phonon Lifetimes in Brillouin Zones,* Physical Review B **91**, 094306 (2015). `doi:10.1103/PhysRevB.91.094306`.

[117] O. Hellman and I. A. Abrikosov, *Temperature-Dependent Effective Third-Order Interatomic Force Constants from First Principles,* Physical Review B **88**, 144301 (2013). `doi:10.1103/PhysRevB.88.144301`.

[118] A. A. Maradudin and A. E. Fein, *Scattering of Neutrons by an Anharmonic Crystal,* Physical Review **128**, 2589 (1962). `doi:10.1103/PhysRev.128.2589`.

[119] A. van Roekeghem, J. Carrete, and N. Mingo, *Anomalous Thermal Conductivity and Suppression of Negative Thermal Expansion in ScF₃,* Physical Review B , 5 (2016).

[120] Q. Zhang, J. Ding, and M. He, *First Principles Study on Structural, Lattice Dynamical and Thermal Properties of BaCeO₃,* Journal of Physics and Chemistry of Solids **108**, 76 (2017). `doi:10.1016/j.jpcs.2017.04.019`.

[121] I. Errea, M. Calandra, and F. Mauri, *Anharmonic Free Energies and Phonon Dispersions from the Stochastic Self-Consistent Harmonic Approximation: Application to Platinum and Palladium Hydrides,* Physical Review B **89**, 064302 (2014). `doi:10.1103/PhysRevB.89.064302`.

[122] P. Souvatzis, O. Eriksson, M. I. Katsnelson, and S. P. Rudin, *The Self-Consistent Ab Initio Lattice Dynamical Method,* Computational Materials Science **44**, 888 (2009). `doi:10.1016/j.commatsci.2008.06.016`.

[123] O. Hellman, I. A. Abrikosov, and S. I. Simak, *Lattice Dynamics of Anharmonic Solids from First Principles,* Physical Review B **84**, 180301 (2011). `doi:10.1103/PhysRevB.84.180301`.

[124] L. T. Kong, *Phonon Dispersion Measured Directly from Molecular Dynamics Simulations,* Computer Physics Communications **182**, 2201 (2011). `doi:10.1016/j.cpc.2011.04.019`.

[125] O. Hellman, P. Steneteg, I. A. Abrikosov, and S. I. Simak, *Temperature Dependent Effective Potential Method for Accurate Free Energy Calculations of Solids,* Physical Review B **87**, 104111 (2013). `doi:10.1103/PhysRevB.87.104111`.

[126] E. Metsanurk and M. Klintenberg, *Sampling-Dependent Systematic Errors in Effective Harmonic Models,* Physical Review B **99**, 184304 (2019). `doi:10.1103/PhysRevB.99.184304`.

[127] A. Stukowski, E. Fransson, M. Mock, and P. Erhart, *Atomicrex—a General Purpose Tool for the Construction of Atomic Interaction Models,* Modelling and Simulation in Materials Science and Engineering **25**, 055003 (2017). `doi:10.1088/1361-651X/aa6ecf`.

[128] J. Behler and M. Parrinello, *Generalized Neural-Network Representation of High-Dimensional Potential-Energy Surfaces,* Physical Review Letters **98**, 146401 (2007). `doi:10.1103/PhysRevLett.98.146401`.

[129] R. Jinnouchi, K. Miwa, F. Karsai, G. Kresse, and R. Asahi, *On-the-Fly Active Learning of Interatomic Potentials for Large-Scale Atomistic Simulations,* The Journal of Physical Chemistry Letters **11**, 6946 (2020). `doi:10.1021/acs.jpclett.0c01061`.

[130] Z. Fan, Z. Zeng, C. Zhang, Y. Wang, K. Song, H. Dong, Y. Chen, and T. Ala-Nissila, *Neuroevolution machine learning potentials: Combining high accuracy and low cost in atomistic simulations and application to heat transport,* Physical Review B **104**, 104309 (2021). `doi:10.1103/PhysRevB.104.104309`.

[131] Y. Lysogorskiy, C. v. d. Oord, A. Bochkarev, S. Menon, M. Rinaldi, T. Hammerschmidt, M. Mrovec, A. Thompson, G. Csányi, C. Ortner, and R. Drautz, *Performant implementation of the atomic cluster expansion (PACE) and application to copper and silicon,* npj Computational Materials **7**, 1–12 (2021). `doi:10.1038/s41524-021-00559-9`.

[132] S. Chmiela, H. E. Sauceda, I. Poltavsky, K.-R. Müller, and A. Tkatchenko, *sGDML: Constructing accurate and data efficient molecular force fields using machine learning,* Computer Physics Communications **240**, 38–45 (2019). `doi:10.1016/j.cpc.2019.02.007`.

[133] S. Batzner, A. Musaelian, L. Sun, M. Geiger, J. P. Mailoa, M. Kornbluth, N. Molinari, T. E. Smidt, and B. Kozinsky, *E(3)-equivariant graph neural networks for data-efficient and accurate interatomic potentials,* Nature Communications **13**, 2453 (2022). `doi:10.1038/s41467-022-29939-5`.

[134] O. T. Unke and M. Meuwly, *PhysNet: A Neural Network for Predicting Energies, Forces, Dipole Moments, and Partial Charges,* Journal of Chemical Theory and Computation **15**, 3678–3693 (2019). `doi:10.1021/acs.jctc.9b00181`.

[135] A. P. Bartók, R. Kondor, and G. Csányi, *On Representing Chemical Environments,* Physical Review B **87**, 184115 (2013). `doi:10.1103/PhysRevB.87.184115`.

[136] D. Frenkel and B. Smit, *Understanding Molecular Simulation: From Algorithms to Applications* (Elsevier Science, 2023). ISBN 9780323913188. `https://books.google.se/books?id=jyipEAAAQBAJ`.

[137] J. G. Kirkwood, *Statistical Mechanics of Fluid Mixtures,* The Journal of Chemical Physics **3**, 300 (1935). `doi:10.1063/1.1749657`.

[138] R. Freitas, M. Asta, and M. de Koning, *Nonequilibrium free-energy calculation of solids using LAMMPS,* Computational Materials Science **112**, 333–341 (2016). `doi:10.1016/j.commatsci.2015.10.050`.

[139] E. Fransson, M. Slabanja, P. Erhart, and G. Wahnström, *Dynasor—A Tool for Extracting Dynamical Structure Factors and Current Correlation Functions from Molecular Dynamics*

Simulations, Advanced Theory and Simulations **4**, 2000240 (2021). `doi:10.1002/adts.202000240`.

[140] J. Cao and G. A. Voth, *The Formulation of Quantum Statistical Mechanics Based on the Feynman Path Centroid Density. I. Equilibrium Properties,* The Journal of Chemical Physics **100**, 5093 (1994). `doi:10.1063/1.467175`.

[141] J. Cao and G. A. Voth, *The formulation of quantum statistical mechanics based on the Feynman path centroid density. II. Dynamical properties,* The Journal of Chemical Physics **100**, 5106–5117 (1994). `doi:10.1063/1.467176`.

[142] M. H. Müser, *Simulation of Material Properties below the Debye Temperature: A Path-Integral Molecular Dynamics Case Study of Quartz,* The Journal of Chemical Physics **114**, 6364 (2001). `doi:10.1063/1.1355772`.

[143] D. A. McQuarrie, *Statistical Mechanics* (Harper & Row, 1976).

[144] G. Grosso and G. P. Parravicini, *Chapter 10 - Scattering of Particles by Crystals,* in *Solid State Physics (Second Edition),* edited by G. Grosso and G. P. Parravicini (Amsterdam: Academic Press, 2014), p. 437. `doi:10.1016/B978-0-12-385030-0.00010-4`.

[145] G. L. Squires, *Introduction to the Theory of Thermal Neutron Scattering* (Cambridge University Press, 2012).

[146] T. Sun, X. Shen, and P. B. Allen, *Phonon quasiparticles and anharmonic perturbation theory tested by molecular dynamics on a model system,* Physical Review B **82**, 224304 (2010). `doi:10.1103/PhysRevB.82.224304`.

[147] A. Carreras, A. Togo, and I. Tanaka, *DynaPhoPy: A code for extracting phonon quasiparticles from molecular dynamics simulations,* Computer Physics Communications **221**, 221 (2017). `doi:https://doi.org/10.1016/j.cpc.2017.08.017`.

[148] A. Rohskopf, R. Li, T. Luo, and A. Henry, *A computational framework for modeling and simulating vibrational mode dynamics,* Modelling and Simulation in Materials Science and Engineering **30**, 045010 (2022). `doi:10.1088/1361-651X/ac5ebb`.

[149] A. H. Romero, E. K. U. Gross, M. J. Verstraete, and O. Hellman, *Thermal conductivity in PbTe from first principles,* Physical Review B **91**, 214310 (2015). `doi:10.1103/PhysRevB.91.214310`.

[150] G. A. S. Ribeiro, L. Paulatto, R. Bianco, I. Errea, F. Mauri, and M. Calandra, *Strong anharmonicity in the phonon spectra of PbTe and SnTe from first principles,* Physical Review B **97**, 014306 (2018). `doi:10.1103/PhysRevB.97.014306`.

[151] O. Delaire, J. Ma, K. Marty, A. F. May, M. A. McGuire, M.-H. Du, D. J. Singh, A. Podlesnyak, G. Ehlers, M. D. Lumsden, and B. C. Sales, *Giant anharmonic phonon scattering in PbTe,* Nature Materials **10**, 614–619 (2011). `doi:10.1038/nmat3035`.

[152] R. Resta and D. Vanderbilt, *Theory of Polarization: A Modern Approach.* In , *Physics of Ferroelectrics* (Berlin, Heidelberg: Springer Berlin Heidelberg, 2007). `doi:10.1007/978-3-540-34591-6_2`.

[153] N. A. Spaldin, *A beginner's guide to the modern theory of polarization,* Journal of Solid State Chemistry **195**, 2–10 (2012). `doi:10.1016/j.jssc.2012.05.010`.

[154] S. Baroni and R. Resta, *Ab initio calculation of the macroscopic dielectric constant in silicon,* Physical Review B **33**, 7017–7021 (1986). `doi:10.1103/PhysRevB.33.7017`.

[155] X. Gonze and C. Lee, *Dynamical matrices, Born effective charges, dielectric permittivity tensors, and interatomic force constants from density-functional perturbation theory,* Physical Review B **55**, 10355–10368 (1997). `doi:10.1103/PhysRevB.55.10355`.

[156] M. Born and K. Huang, *Dynamical theory of crystal lattices* (Clarendon Press, 1954).

[157] R. A. Cowley, *The theory of Raman scattering from crystals,* Proceedings of the Physical Society **84**, 281–296 (1964). `doi:10.1088/0370-1328/84/2/311`.

[158] M. Cardona, *Resonance phenomena* (Springer, 1982). ISBN 978-3-540-11380-5. `doi:10.1007/3-540-11380-0`.

[159] W. Willes H. and M. Roberto, eds., *Raman Scattering in Materials Science* (Springer, 2000). ISBN 978-3-642-08656-4. `doi:10.1007/978-3-662-04221-2`.

[160] M. Cardona, ed., *Light Scattering in Solids I* (Springer, 1983). ISBN 978-3-540-11913-5. `doi:10.1007/3-540-11913-2`.

[161] E. Fransson, F. Eriksson, and P. Erhart, *Efficient Construction of Linear Models in Materials Modeling and Applications to Force Constant Expansions,* npj Computational Materials **6**, 1 (2020). `doi:10.1038/s41524-020-00404-5`.

[162] A. J. Smola and B. Schölkopf, *A Tutorial on Support Vector Regression,* Statistics and Computing **14**, 199 (2004). `doi:10.1023/B:STCO.0000035301.49549.88`.

[163] M. E. Tipping, *Sparse Bayesian Learning and the Relevance Vector Machine,* The Journal of Machine Learning Research **1**, 211 (2001). `doi:10.1162/15324430152748236`.

[164] L. J. Nelson, V. Ozoliņš, C. S. Reese, F. Zhou, and G. L. W. Hart, *Cluster Expansion Made Easy with Bayesian Compressive Sensing,* Physical Review B , 10 (2013). `doi:10.1103/PhysRevB.88.155105`.